

## Article

# A Critical Analysis of Helical and Linear Channel Liquid Cooling Designs for Lithium-Ion Battery Packs

Rob Lloyd and Mohammad Akrami \*

Department of Engineering, University of Exeter, Exeter EX4 4QF, UK

\* Correspondence: m.akrami@exeter.ac.uk

**Abstract:** Thermal management systems are integral to electric and hybrid vehicle battery packs for maximising safety and performance since high and irregular battery temperatures can be detrimental to these criteria. Lithium-ion batteries are the most commonly used in the electric vehicle (EV) industry because of their high energy and power density and long life cycle. Liquid cooling provides superior performance with low power draw and high heat transfer coefficient. Two liquid cooling designs—the Linear Channel Design (LCD) and Helical Channel Design (HCD)—underwent multiple numerical and geometrical optimisations, where inlet mass flow rate, channel diameter, and inlet and outlet locations were analysed using CFD (computational fluid dynamics). The primary objectives were to maintain maximum temperatures and thermal uniformity within the operational limits derived from the literature. These were both achieved with the LCD using a mass flow rate of  $7.50E-05 \text{ kgs}^{-1}$ . The  $T_{\max}$  goal was met for the HCD but not the thermal uniformity goal. The LCD achieved 1.796 K lower in maximum temperature and 8.740 K lower in temperature difference compared to the HCD, proving itself superior in both metrics. The HCD required a higher mass flow rate than the LCD to regulate temperatures, resulting in an undesirably high power consumption.



**Citation:** Lloyd, R.; Akrami, M. A Critical Analysis of Helical and Linear Channel Liquid Cooling Designs for Lithium-Ion Battery Packs. *Batteries* **2022**, *8*, 236. <https://doi.org/10.3390/batteries8110236>

Academic Editors: Jinsheng Xiao, Hengyun Zhang, Soussou Kelouwani and Torsten Brezesinski

Received: 12 September 2022

Accepted: 9 November 2022

Published: 12 November 2022

**Publisher's Note:** MDPI stays neutral with regard to jurisdictional claims in published maps and institutional affiliations.



**Copyright:** © 2022 by the authors. Licensee MDPI, Basel, Switzerland. This article is an open access article distributed under the terms and conditions of the Creative Commons Attribution (CC BY) license (<https://creativecommons.org/licenses/by/4.0/>).

**Keywords:** lithium-ion battery; thermal management; liquid cooling; linear channel; helical channel; design optimisation; electric vehicle

## 1. Introduction

### 1.1. Background

With ever-increasing concern for pollution due to the use of fossil fuels, the demand for electric and hybrid vehicles has noticeably been on the incline in recent years. In 2015, 65% of global oil consumption was due to the transport sector [1], and in 2021, a declaration was made at COP26 (the UN climate change conference) entailing the sales of all new cars and vans to be zero emission vehicles globally by 2040 and by no later than 2035 in leading markets [2], meaning that developments for sustainable EV (Electric Vehicle) technology are in high demand by automotive companies.

Lithium-ion batteries have been a popular choice within the industry for EV powertrains due to their high energy density, high power density and long life cycle [3]. When lithium-ion batteries undergo the discharge cycle during operation, they generate a considerable amount of heat that needs to be expelled, because high and irregular temperatures can severely impact the battery pack's performance, life cycle and safety [4]. The main aim of this research is, therefore, to provide a suitable and effective thermal management system for the use of EV battery packs. The criteria needed to reach this aim include maintaining the maximum temperature of the cells within the optimal operating range of  $298 \text{ K} < T_{\max} < 313 \text{ K}$  [5] and the thermal uniformity of the cells in the form of temperature difference in the range of  $\Delta T < 5 \text{ K}$  [5]. Thermal uniformity is an important metric for analysing thermal performance due to the application of the Arrhenius law [6], where areas of high cell temperature increase the current and accelerate electrochemical reactions, causing a local peak SOC (State of Charge). Uneven SOCs within electrodes shorten the operating lifespan of the cell by

accelerating the ageing of the electrodes at high SOCs [6]. Furthermore, the thermal management solution should be realistic for use in an EV and not consume unnecessarily large quantities of power in order to operate that would otherwise be more usefully diverted to other systems in the vehicle. Additionally, the cost and manufacturing complexity will be minor factors to consider towards the end of the design optimisation process. These criteria will be achieved through a series of numerical and geometrical optimisations to the given designs.

## 1.2. Literature Review

Over the past decade, extensive research has been conducted on EV lithium-ion battery packs' thermal management systems. The demand for new innovative ways to improve battery performance from various electric car manufacturers, has always been prevalent due to cooling being a major factor in the vehicle's overall performance and efficiency. This literature review will be categorised in order to cover the three key areas of EV battery pack cooling research, comprising PCM cooling, air cooling and liquid cooling.

### 1.2.1. PCM Cooling

One of the fundamental areas for research within the thermal management of EV battery packs involves the use of a PCM enclosure for the Li-ion cells. PCM cooling relies on the absorption and release of thermal energy when the coolant material changes phase. PCMs have been explored in recent research such as that of Li et al. [7] where porous cellulose nanofibril (CNF)/silver nanowire (AgNW) hybrid supporting materials were used to increase the phonon propagation of the cellulosic material lattice and improve the thermal transmission ability of the hybrid carriers.

Multiple structural arrangements of PCM enclosures have been proposed in the literature, such as Choudhari et al. [8] comparing the use of rectangular, triangular, trapezoidal, I-shape and T-shape fins within the PCM enclosure in order to counteract the heat accumulation in PCMs due its low heat conduction [8]. It was concluded that the I-shape and rectangular fins had the strongest performance in terms of maximum temperature reduction and thermal uniformity. Although it should be said that each of these fin types had very similar results, leading to the conclusion that fin shape is not a major determining factor in the performance of a battery thermal management system. Additionally, this test was conducted on a single Li-ion battery and not a pack, which may limit the usefulness of this data for car manufacturers, so a battery pack should be tested for future research. Landini et al. [9] studied the use of direct-metal-laser-sintered aluminium heat exchangers containing PCMs, finding that the system showed promising results in comparison to natural convection and maintained an even thermal uniformity.

An interesting development in the research of PCM cooling involves the combination with liquid cooling, as researched by Cao et al. [10], who proposed a structure containing EG/RT44HC acting as a PCM alongside a cold plate situated in amongst the battery pack. It was found that in order to best control the battery pack's thermal performance, the coolant water temperature should be limited to less than 313K and as close to the ambient temperature as possible [10]. It was found that these low inlet temperatures reduce the general temperature of the battery pack but increase the temperature in the axial and radial directions, worsening the thermal uniformity of the Li-ion cells. Hekmat et al. [11] investigated a hybrid PCM and liquid-cooled structure for prismatic cells, finding that the PCM was especially beneficial in creating a strong thermal uniformity. The addition of coolant pipes reduced the maximum temperature significantly compared to singularly using PCM, indicating that liquid cooling systems will majorly influence the thermal performance of an EV battery pack. Perhaps the liquid cooling structures should be researched heavily to optimise cooling performance instead of purely relying on passive cooling.

### 1.2.2. Air Cooling

The use of natural convection (air cooling) is commonly used for effectively managing the thermal performance of an EV battery pack. Fans are generally used in practice [12] as opposed to purely relying on the exterior winds around the moving vehicle which would be unreliable and not keep temperatures steady enough over an extended period of time. Air cooling systems for EV battery packs are generally cheaper and simpler in design when compared to liquid cooling loops [12]. However, some issues can arise in terms of the thermal uniformity of Li-ion cells since predicting the exact flow path of the air and making sure it evenly cools each Li-ion cell can be troublesome to model, which is why much literature has focused on this, along with minimising maximum temperatures.

Forced air cooling systems have been developed by scholars such as Wang et al. [13], where two cooling channels were used and tested at multiple discharge rates. Results showed that the cooling efficiency reached 73%, and the maximum temperature decreased from 343 K to 328 K at a discharge rate of 1C. The main appeal of this design is the alternating airflow system, which has a noticeably beneficial impact on the thermal uniformity of the battery pack. However, it had a negligible effect in reducing maximum temperatures. The idea of alternating inlet airflow arrangements was also researched by Sharma et al. [14], with the conclusion that dual-direction airflow provided great benefits to thermal uniformity and required a lower power consumption compared to unidirectional airflow. The airflow velocity was also optimised to be  $2 \text{ ms}^{-1}$  for 1, 2 and 3C discharge rates and  $4 \text{ ms}^{-1}$  for 4C.

The battery pack structure and layout of the cells are important considerations and determining factors when it comes to the thermal performance of an EV battery pack. Xi et al. [15] proposed a novel Z-type structure, which produced promising results for thermal performance when an optimisation process was conducted. Furthermore, the addition of deflectors and rounding-off chamfers reduced the maximum temperature by 2.52 K and enhanced the thermal uniformity due to the more balanced airflow within the battery pack. A J-type airflow structure was studied by Liu et al. [16] with a comparison to U-type and Z-type structures. It was found that after the J-type system was optimised using surrogate-based optimisation, it showed a 4.12 K reduction in maximum temperature in relation to the U-type system and a 15.42 K reduction compared to the Z-type structure since the optimised system benefits from a highly balanced and uniform airflow distribution.

### 1.2.3. Liquid Cooling

Liquid cooling is the method of EV battery thermal management employed by car manufacturers such as Tesla, BMW and Ford [17] and is the most widely researched in the literature, with many different types of designs. It should be noted that liquid cooling can be split into direct and indirect cooling, where the former involves the submersion of the Li-ion cells directly into the coolant fluid. While direct cooling comes with the advantages of maximal thermal contact area for the cells and greatly improved thermal uniformity [12], this method is uncommon in the real-world manufacturing of battery thermal management systems. This is due to the troublesome requirement of the water-resistant performance of the battery pack, where electrical short circuits and electrochemical reactions may occur [12]. This is why indirect liquid cooling (designs involving exterior channels for coolant flow) is a well-researched area in the literature and is held at a higher degree of importance by both scholars and EV manufacturers.

Car manufacturers such as Tesla make use of a serpentine wavy channel cooling structure, which a fair level of academic research has been conducted on, such as Zhao et al. [18], that used a simulation of a serpentine channel cooling arrangement battery pack. The pack comprises 71 18,650 Li-ion cells, where the heat generation is based on experimental data of a single cell. Zhao et al. [18] found that increasing the discharge/charge rate of the cells increases the battery pack temperature and worsens its thermal uniformity and increasing the coolant flow rate significantly lowers the temperature and improves thermal uniformity. However, this was only tested with two inlet velocity rates,  $0.1 \text{ ms}^{-1}$

and  $0.5 \text{ ms}^{-1}$ , providing very little sample space, so there is room to research and find an optimal flow rate. Zhao et al. [18] also found that modelling a contact area between each cell had a negligible effect on the thermal performance and that increasing the contact area between each cell and the coolant loop resulted in lower battery pack temperatures (due to the increase in contact surface area resulting in a higher rate of thermal dissipation). Although, again this was tested arbitrarily with contact angles of  $10^\circ$ ,  $20^\circ$ ,  $30^\circ$  and  $40^\circ$ , so an optimal or maximum can still be researched.

The following year, this research was built upon again by Zhao et al. [19], with the main focus being to optimise thermal uniformity with the battery pack. The removal of the coolant loop's U-turn resulting in multiple single wavy channels was tested, with the findings that this improved the thermal uniformity and reduced the maximum temperature of the battery pack. This time, the contact area of the cell and coolant loop was tested much more in-depth. It was found that increasing the contact area improved thermal uniformity. The serpentine wavy cooling channel structure was also researched by Xu et al. [20], comparing it with a U-shaped coolant loop with grooves. It was found that the serpentine wavy structure had better performance in terms of maximum temperature reduction, that being  $0.37 \text{ K}$  lower than the U-shaped structure, and demonstrated a better thermal uniformity. It would be potentially useful to combine the research of Zhao et al. [18] and Xu [19] to test a single-channel system with grooves.

In terms of alternative liquid cooling structures, many novel designs have been proposed in the literature that are not similar to those currently adopted by car manufacturers, such as the use of a helical duct structure encasing each Li-ion cell. Multiple parameters within this design were tested by Zhao et al. [21], and it was found that the battery pack's maximum temperature was lowered, and the temperature uniformity was improved as the inlet mass flow rate increased, concurring with the findings of Zhao et al. [18] even for a vastly different coolant structure. It was also discovered that when the pitch and number of helical ducts were varied on the optimal flow rate model of  $3 \times 10^{-4} \text{ kgs}^{-1}$ , this had a negligible effect on the thermal performance of the battery pack. Various cases of alternating fluid flow were tested in an attempt to regulate temperature (since outlet temperature will inevitably be lower than inlet temperature). The findings highlight that having three inlets and two outlets at the positive electrode of the battery gave a  $T_{\max}$  of  $306.95 \text{ K}$  and  $\Delta T$  of  $7.4 \text{ K}$  at 40% DOD compared to a  $T_{\max}$  of  $307.85 \text{ K}$  and  $\Delta T$  of  $8.7 \text{ K}$  for a one inlet, four outlet case. This technique improved cooling effectiveness and thermal uniformity when the fluid flow is alternated. Finally, the helical duct diameters were tested with the conclusion that smaller diameter ducts result in slightly lower maximum temperatures but a worsened thermal uniformity.

The use of helical liquid ducts was also researched by Dong et al. [22], who analysed a novel double helix structure. It was also found that an increase in coolant mass flow rate resulted in lower maximum temperatures. Although in this paper, a wider sample was used in order to derive a converging relationship, where the cooling benefits of higher mass flow rates began to diminish as the flow rate increased beyond  $5 \times 10^{-4} \text{ kgs}^{-1}$ . The pitch and diameter parameters were also tested, with the conclusion concurring with the findings of Zhao et al. [21] that the smaller diameters result in lower maximum temperatures but a worsened thermal uniformity.

The use of linear mini-channel cooling structures has been a key area of EV battery liquid cooling research over recent years, with many design variations being proposed and evaluated in the literature. Some designs have linear channels flowing perpendicular to the length of the cells, such as the structure proposed by Rao et al. [23], comprising aluminium blocks between the Li-ion cells with mini channels for coolant flow. The particular design shown in this paper provides adequate cooling performance for the battery pack since the temperatures are kept well within operating conditions. However, it is obvious from the schematics of this design that since the straight mini-channels flow perpendicular to the lengths of the Li-ion cells, the thermal uniformity of the cells is weakened. This is mainly due to the distance between a given coolant channel and the cells is constantly

changing along the length of the channel. This is evident in the results of Rao et al. [23], where the temperature contours demonstrate large variation within the cell volumes. This can be a major issue as denoted by Zeng et al. [6], where the volumetric heat generation rate increases with the energy density and charge rate. There is more battery heat to be dissipated, requiring more cooling power. Zeng et al. [6] mentions the application of the Arrhenius law, where areas of high cell temperature increase the current and accelerate electrochemical reactions, causing a local peak SOC. Uneven SOCs within electrodes shorten the operating lifespan of the cell by accelerating the ageing of the electrodes at high SOCs. From this, the thermal uniformity of the Li-ion cells shall be an important consideration for the proposed designs in this paper.

Most of the proposed linear cooling channel designs within the literature comprise channels parallel to the lengths of the cells. Lai et al. [24] researched designs in this area and identified a gap in the literature research, being the lack of focus on the weight and compactness of the battery pack, which is an important factor for the performance of electric vehicles. A lightweight battery pack was constructed comprising multiple aluminium thermal conductive structures containing coolant channels, allowing the cooling water to flow from an upper reservoir and down the lengths of each cell to the lower reservoir. It was also stated that liquid cooling, in general, provided far superior heat transfer coefficient and power consumption levels in relation to PCM and air cooling. A similar concept was presented by Sheng et al. [25], utilising a cellular liquid cooling jacket. Sheng et al. [24] discovered that interlaced flow directions provide a lower temperature standard deviation and improved thermal uniformity, concurring with the findings associated with the helical channel designs of Zhao et al. [21]. A glycol aqueous solution was also tested, with the conclusion that this is a more effective coolant than regular liquid water. Although, there is still room to potentially test more coolants to fully optimise this design.

Another such design would be the mini channel cylinder cooler proposed by Zhao et al. [26]. Similar to the design proposed by Lai et al. [24], the battery pack comprises an upper and lower reservoir connected via vertical ducts for the coolant to flow along the length of the cells. However, this design makes use of smaller channels (0.8 mm diameter) compared to that of the design proposed by Lai et al. [24] (2 mm diameter), and utilises up to sixteen channels surrounding each cell as opposed to three per cell from Lai et al. [24]. Zhao et al. [26] and Lai et al. [24] made use of different form factors of Li-ion batteries, 42,110 and 18,650, respectively. Comparing cooling performance among these designs provide little analytical benefit, so perhaps a comparison of these designs under the same boundary conditions and using the same battery form factor should be studied in future studies.

With liquid cooling showing very promising results within this field of research, the aim of this study shall be to further develop the specific types of cooling loops used within the literature. A comprehensive evaluation shall be conducted to determine the applicability of each design, to encourage further research for the superior model.

## 2. Materials and Methods

### 2.1. Battery Chemistry

On a basic level, the purpose of a battery is to convert chemical energy to electrical energy via an electrochemical oxidation-reduction reaction, for which the inverse of this reaction is used to recharge a rechargeable battery. This type of reaction involves the transfer of electrons from one material to another through an electric circuit [27]. The batteries store and discharge energy in the form of charged atoms or ions, and the charge and discharge rate of the battery is restricted by the speed that ions can move through the cell [28].

A typical cell comprises three primary components:

1. The anode—gives up electrons to the external circuit and is oxidized during the electrochemical reaction [26].
2. The cathode—accepts electrons from the external circuit and is reduced during the electrochemical reaction [26].

3. The electrolyte—is usually a liquid medium to sustain ionic conductivity and transfer ions between the cathode and anode.

In order to maximise the efficiency of the battery, the materials for the anode and cathode should be light and provide high cell voltage and high capacity [27]. The metal with the lowest density on the periodic table is lithium, which also has a high electrochemical potential, making this a logical choice for the production of batteries. Research into intercalation electrodes has led to the use of lithiated carbons and lithium alloys in lithium-ion technology [27]. There are many different types of lithium-ion batteries, such as LiCoO<sub>2</sub>, LiFePO<sub>4</sub>, LiMn<sub>2</sub>O<sub>4</sub>, LiNiMnCoO<sub>2</sub> and Li<sub>2</sub>TiO<sub>3</sub>. Each of these types comes with its own benefits and drawbacks. LiCoO<sub>2</sub> is the most commonly used form of lithium-ion battery, and is under consideration for use in innovative solid-state batteries [29]. The LiFePO<sub>4</sub> battery uses lithium iron phosphate as the cathode material and in comparison to LiCoO<sub>2</sub>, has a lower energy density, longer lifetime, and higher power density [27]. A study performed by Tang et al. [30] showed that under external heating conditions, the LiFePO<sub>4</sub> battery was able to withstand a higher heat until failure compared to both the Li<sub>2</sub>TiO<sub>3</sub> and LiNiMnCoO<sub>2</sub> batteries, proving itself superior in thermal stability. Developments have recently been made using a silicon anode for solid state lithium-ion batteries such as Gu et al. [31], where a novel SiO<sub>2</sub>@Li<sub>3</sub>PO<sub>4</sub>@carbon shell coated on micron-sized silicon was shown to maintain mechanical integrity and stable cycling performance with high capacities. Han et al. [32] also demonstrated the benefits of a novel silicon MXene with interfacial nitrogen engineering, which also achieved high mechanical stability as well as stable and fast lithium-ion transportation pathways. Both of these silicon-based anodes could potentially be incorporated into the proposed thermal management systems in this study, although requiring a moderate reconstruction of geometries to account for dimensional changes. Table 1 shows data for the lithium iron phosphate battery modelled in this study [27,28,33].

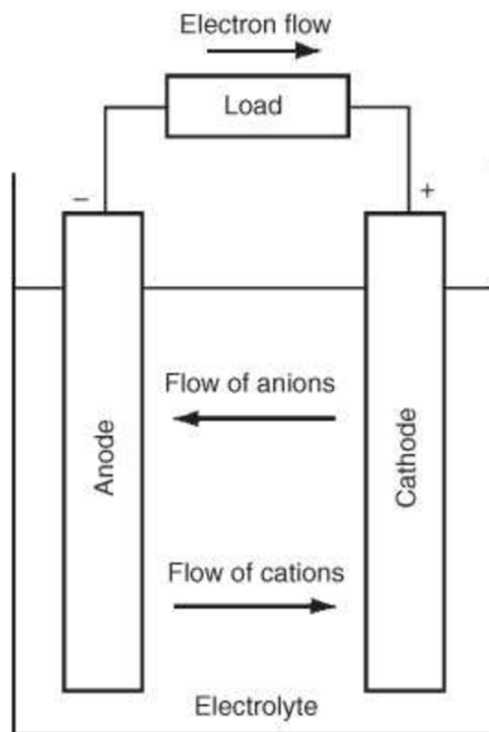
**Table 1.** Lithium Iron Phosphate battery properties.

Battery	Cell Voltage (V)	Specific Energy (MJkg <sup>-1</sup> )	Cycle Life (Cycles)	Charge Rate (Hours)
Lithium Iron Phosphate (LiFePO <sub>4</sub> )	3.3	>0.32	1000+	<1

Under extreme conditions, the safety of a lithium-ion battery can be compromised, for example during a short circuit, when temperatures can increase rapidly [34]. The use of hydrogel to rapidly absorb thermal energy and mitigate thermal runaway when was explored to a high degree of success by Zhao et al. [34]. Collisions are also a major risk to the battery pack integrity and safety, for which shock-absorbing “sacrifice” tubes and crushable foam were tested by Kukreja et al. [35] and were successful in reducing the severity of collisions.

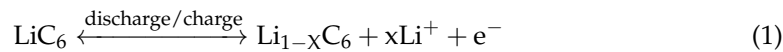
When a battery is under operational use, it is undergoing its discharge cycle. For practical purposes, the performance efficiency of batteries is often rated not on a full discharge cycle, but instead using a percentage of DOD (Depth of Discharge), since batteries are seldom fully discharged due to long term damage this could cause to the batteries.

Figure 1 shows a typical representation of the discharge process of a cell. It can be seen that the electron flow takes place from the oxidised anode to the cathode via the external load. As the electrons are received by the cathode, the cathode material is gradually depleted. Anions (negative) flow from the cathode to the anode, and cations flow vice versa through the electrolyte to complete the circuit. Over the charging cycle of a rechargeable battery, the flow of current is reversed, and the anode and cathode switch places to become the positive and negative electrodes, respectively. The electrochemical reactions during both of these processes are represented by Equations (1) and (2) [26]:

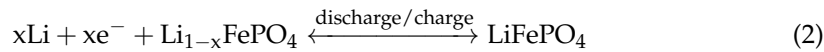


**Figure 1.** Discharge process of a cell [26].

Anode:



Cathode:



## 2.2. Numerical Model

In this investigation of liquid-cooled battery pack thermal management systems, the computational fluid dynamics (CFD) method is introduced, where it is important to understand the governing equations behind the simulation of lithium-ion batteries and the energy transfer due to the liquid cooling channels. First of all, the heat generation of a single lithium-ion cell was modelled according to the following Equation (3) [36]:

$$\frac{\partial}{\partial t} \left( \rho_b \cdot c_{p,b} \cdot T_b \right) = \nabla \cdot (k_b \cdot \nabla T_b) + q_{\text{gen}} \quad (3)$$

where  $\rho_b$  is the generalised density of the battery,  $c_{p,b}$  is the specific heat capacity of the battery,  $k_b$  is the generalised thermal conductivity of the battery, finally  $q_{\text{gen}}$  is the heat generation of the battery and can be determined by [21]:

$$q_{\text{gen}} = \frac{Q_b}{V_b} \quad (4)$$

where  $Q_b$  is the rate of heat flow across the battery and  $V_b$  is the volume of the battery. Much work relating to lithium-ion battery heat generation within recent literature has been based upon the work of Bernardi et al. [37], for which a simplified Bernardi equation is used within this research and is as follows [38]:

$$q_{\text{gen}} = \frac{1}{V_b} \left[ I_b^2 R_b + I_b T_b \frac{dU_b}{dT} \right] \quad (5)$$

where  $dU_b/dT$  refers to the temperature coefficient, a parameter related to the electrochemical reaction within a lithium-ion cell derived from the open-circuit voltage of the battery,  $U_b$ .  $I_b$  is the current through the battery and  $R_b$  is the internal resistance of the battery. The coolant used within this research was liquid water, for which the fluid flow and heat transfer model can be expressed using the three following equations [21], firstly the continuity equation [21]:

$$\frac{\partial \rho_w}{\partial t} + \nabla \cdot (\rho_w \vec{v}_w) = 0 \quad (6)$$

where  $\rho_w$  is the density of water,  $t$  is time and  $\vec{v}_w$  is the velocity of the water. The momentum conservation equation [21]:

$$\frac{\partial \vec{v}_w}{\partial t} + (\vec{v}_w \cdot \nabla) \vec{v}_w = -\frac{1}{\rho_w} \nabla \cdot P + \mu_w \nabla^2 (\vec{v}_w) \quad (7)$$

where  $P$  is pressure,  $\mu_w$  is the dynamic viscosity of water. Lastly, the energy conservation equation [21]:

$$\frac{\partial}{\partial t} (\rho_w \cdot c_{p,w} \cdot T_w) + \nabla \cdot (\rho_w \cdot c_{p,w} \cdot \vec{v}_w \cdot T_w) = \nabla \cdot (k_w \nabla T_w) \quad (8)$$

where the aforementioned variables are associated with water denoted by subscript "w". The heat transfer between the coolant, aluminium channels and the battery can be modelled through the following heat flow equations:

$$Q = \dot{m} \cdot c_p \cdot \Delta T \quad (9)$$

$$Q = h \cdot A \cdot \Delta T \quad (10)$$

where  $\dot{m}$  is the mass flow rate,  $h$  is the heat transfer coefficient and  $A$  is the contact area for heat transfer. When dealing with fluid flow, the distinction between laminar, transitional and turbulent flow is important to consider and is characterised by the Reynolds number:

$$Re = \frac{\rho v L}{\mu} = \frac{4\dot{m}}{\pi L \mu} \quad (11)$$

The properties of the materials used in this investigation are summarised in Table 2, for which the properties of aluminium and liquid water were sourced directly from the materials database in ANSYS Fluent. The properties of the battery are sourced from the work of Zhao et al. [4] and are assumed to be uniform throughout the geometry of the battery.

**Table 2.** Material properties.

Materials	$\rho$ ( $\text{kg m}^{-3}$ )	$c_p$ ( $\text{J kg}^{-1} \text{K}^{-1}$ )	$k$ ( $\text{W m}^{-1} \text{K}^{-1}$ )	$\mu$ ( $\text{kg m}^{-1} \text{s}^{-1}$ )
Liquid water	998.2	4128	0.6	$1.003 \times 10^{-3}$
Aluminium	2719	871	202.4	-
Battery	1760	1108	3.91	-

### 2.3. Modelling a Single Lithium-Ion Cell

There are many different types of lithium-ion batteries to consider for study such as cylindrical, prismatic and pouch. The LiFePO<sub>4</sub> cylindrical lithium-ion battery was selected for modelling, given this has shown promising electrochemical and thermal characteristics as described earlier, and there has been a recent wave in the EV manufacturing industry to mass adopt this particular battery chemistry [39]. Many form factors for cylindrical batteries exist, such as 18,650, 21,700 and 4680. The numbering system is characterised by the dimensions of the battery. For example, the 18,650 battery is 18 mm in diameter

and 65 mm in height. The new “tabless” 4680 batteries, which are still in development by Tesla, were originally considered for study. Although this, unfortunately, means that there is limited technical information available to the general public and academic scholars, which would make the heat generation model of the battery impossible to validate. This is why the 18,650 form factor was eventually chosen for study, given there is plenty of technical information available about this battery in the literature as summarised in the literature review.

Firstly, the heat generation of a single cell undergoing its discharge cycle must be accurately modelled to produce meaningful results. The geometry for a simple 18,650 cylindrical lithium-ion cell was created in SolidWorks 2021 (Dassault Systèmes, SolidWorks Corp., Waltham, MA, USA) with the relevant dimensions of 18 mm diameter and 65 mm height and was imported into ANSYS Fluent (ANSYS Inc., Canonsburg, PA, USA) as a step file. The applied material properties are shown in Table 2 and are assumed to be uniform throughout the geometry of the battery. This would provide a limitation to the accuracy of the battery model since different components of the battery, such as the can, separator, cathode, and anode foil, would all comprise unique material properties, but for the purpose of this study, a generalised material composition provides accurate enough data without compromising on highly complex geometry and computational power requirements.

Papers covered in the literature review, as well as other research in this field, use the experimental results of Wang et al. [40], for which a cell operated at a 5C discharge rate achieved a maximum temperature of 351 K after 720 s, and where the heat generation and temperature of the cell increased approximately linearly with respect to time throughout the 720 s discharge cycle. Furthermore, from the results of Wang et al. [34], it was shown that as the discharge rate was increased, the heat generated in the battery was greater. For this study, the single cell model was given a heat generation rate of  $q_{gen} = 138,000 \text{ W m}^{-3}$  within the cell zone conditions and set to run transiently for 720 s. At the end of the discharge cycle, the cell reached a maximum temperature of 351 K through a linear increase in temperature with respect to discharge time (shown in Figure 2), validating this thermal model against the literature. Given this was a very simple calculation for Fluent with simple geometry, different mesh densities provided infinitesimal differences in results, so a mesh dependency study provides little analytical benefit here. Mesh dependency will become significant for the full simulated battery packs with cooling, given the higher complexity of the problem.

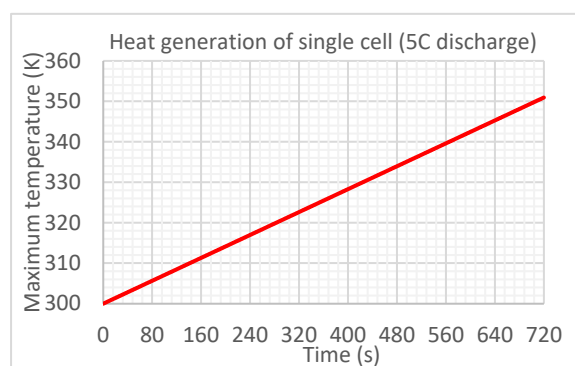


**Figure 2.** Heat generation of a single cell (5C).

#### 2.4. Construction of the Linear Channel Design (LCD) Battery Pack

The first proposed liquid cooling design is one based upon the work of Lai et al. [24], where SolidWorks 2021 was used in order to plan the design for and build the CAD model, shown in Figure 3 (all dimensions shown are in mm). The LCD considers a pack of four lithium-ion cells to alleviate computational power requirements, with nine coolant flow channels, as presented in Figure 3c. The channels each have four curved edges that interlock with the cylindrical cell surfaces, and the upper reservoir carries fluid from the

inlet through the channels to the outlet on the lower reservoir. As opposed to the staggered battery arrangement with three contact surfaces per channel proposed by Lai et al. [24], the LCD uses a uniform structured battery arrangement with four contact surfaces per channel to provide a more useful comparison to the HCD. This is covered in the next section. It should be noted that this arrangement of batteries is slightly less compact, providing a minor limitation to the usefulness of this design within an EV. The channel diameter and the inlet and outlet locations were chosen arbitrarily for now, as they are to be optimised later in this study, as well as the inlet mass flow rate.

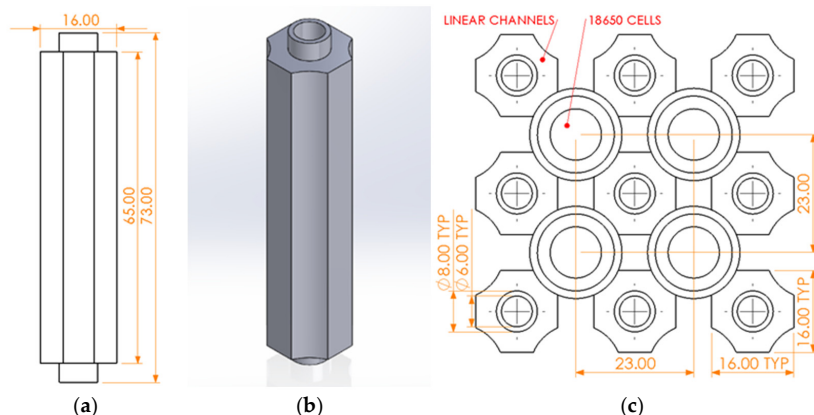


**Figure 3.** LCD views and dimensions, all in millimetres: (a) Single channel side view; (b) Single channel ISO view; (c) Battery pack top view with fluid domain removed.

## 2.5. Construction of the Helical Channel Design (HCD) Battery Pack

The second proposed liquid cooling design is one based upon the work of Zhou et al. [21] and Dong et al. [22], involving helical coolant channel structures weaving around each cell. Ideally, the main benefit of a helical channel structure should be the allowance for a more even distribution of coolant around the circumference of the cell, improving thermal uniformity. The CAD model created in Solidworks 2021 is presented in Figure 4 (all dimensions in mm). Illustrated in Figure 4, a helix was swept, and an extruded cylindrical cut of radius 9 mm was taken through the centroid, creating a half helix structure similar to the work of Zhou et al. [21]. This allows the lithium-ion cell to have a maximal contact area with the helical channel via a continuous flat edge, allowing for the greatest quantity of heat transfer rate, as described in Equation (10). The HCD also comprises four lithium-ion cells which are spaced in the same arrangement as the LCD, to provide the most relevant comparison. Each cylindrical cell has its own helical channel, for which the coolant flows from the inlet into the upper reservoir and through the helical channels to the outlet on the lower reservoir.

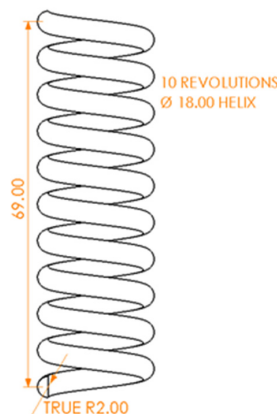


**Figure 4.** Helical channel–side (mm).

## 2.6. CFD Configuration and Boundary Conditions

Once each battery pack assembly had been created in SolidWorks 2021, they were imported as a step file into ANSYS 2021 R1. A hexahedral mesh was generated for each battery pack within ANSYS Mechanical. This provided low numerical diffusion, resulting in a solution of higher accuracy [41] compared to meshing geometries such as tetrahedral. Body and face sizings were applied to enhance the mesh density of critical areas of heat transfer, such as the channels and sections of the fluid domain, as well as inflation layers between the boundaries of the fluid, channel and batteries. Inflation layers are vital for resolving the boundary layer between two regions where a significant temperature gradient is occurring due to energy imbalance. The first layer thickness was set to 0.1 mm based on the  $y+$  value of 1 [42], with a growth rate of 1.2. It is generally good practice with inflation layers to include between 10 and 15 layers to accurately resolve the boundary layer and predict separation or reattachment points [43], which is why 10 layers have been used for these studies. According to the Fluent User's Guide [44], the orthogonal quality should be kept close to 1 and skewness close to 0 (perfectly equiangular cells), which was confirmed for every case and geometrical optimisation using the mesh statistics in ANSYS Mechanical. Lastly, the named selections are applied to the relevant geometries for ease of access within Fluent.

In Fluent, the double precision mode was activated to provide more accurate simulations, and the transient model was selected. The energy model was activated to allow the equations of heat transfer Equation (8), along with the 2-equation  $k-\epsilon$  turbulence model. Liquid water was used as the coolant in this study, which is commonly used in the literature, and a custom material was created for the battery using the properties described in Table 2. The appropriate materials were assigned in the cell zone conditions: aluminium for the channels, liquid water for the fluid domain and the custom battery material for the lithium-ion cells. The heat generation model described earlier is applied here for the cells. The fluid inlet boundary condition is set to 300 K and as a mass flow inlet, initially as  $2.5 \times 10^{-5} \text{ kgs}^{-1}$ , well within the laminar flow region as described by Equation (12) (derived from Equation (11), using 8 mm as the inlet diameter and the dynamic viscosity of water from Table 2).

$$\dot{m}_{\max} = \frac{\text{Re} \cdot \pi \cdot L \cdot \mu}{4} = \frac{2300 \times \pi \times 8 \times 10^{-3} \times 0.001003}{4} = 0.0145 \text{ kgs}^{-1} \quad (12)$$

Any walls separating fluid or solid domains were set as coupled, allowing natural convection for energy transfer, and the interior faces of the channels were set to a no-slip condition and as stationary. The ambient conditions are 300 K, and each case was assumed to be in an adiabatic environment via the battery pack exterior surfaces set to thermally insulating boundaries, due to the constricted airflow in real EV battery pack environments where the thermal impact is negligible. As each optimisation is completed in this study, the newfound boundary conditions are applied for the consecutive stages.

Monitors were set to record the maximum and minimum temperatures for the volumes of the lithium-ion cells over time, and a hybrid initialisation was utilised. For the calculation, each time step was set to a magnitude of 1 s for 720 time steps in order to recreate the 5C discharge cycle [40], as described earlier. The maximum iterations per time step was set to 300 in order to significantly increase the likelihood of convergence, although it was found that most time steps converged between 1 and 10 iterations.

## 2.7. Mesh Dependency

A mesh refinement study was performed on the LCD and HCD to find convergence in the solution where an optimal mesh can be applied to provide accurate solution data without extending the computational time and power requirements unreasonably. This is achieved by gradually applying denser element meshing via altering the global mesh size, the body and face sizing, and inflation layers. The results were recorded in each case (in this case, the maximum temperature of the cells), and the graphs presented in Figure 5

show the convergences. The data was plotted on separate graphs for clarity. Since the data range for  $T_{\max}$  in each case is small, the graphs would appear as almost horizontal lines otherwise.

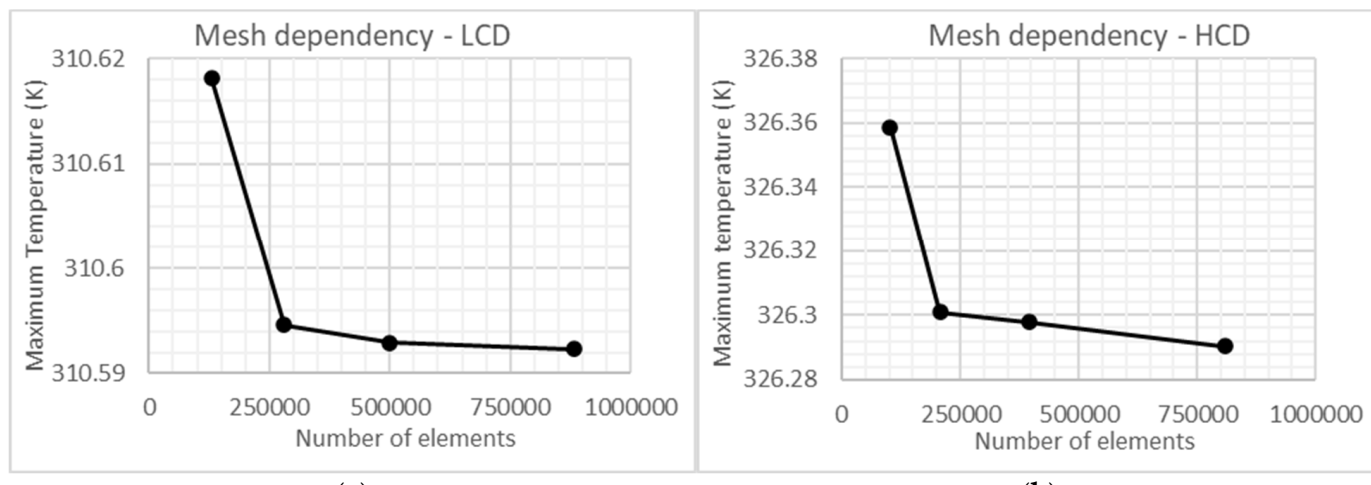


**Figure 5.** Mesh dependency study for the: (a) LCD; (b) HCD.

From Figure 5a, it can be seen that the maximum temperature of the lithium-ion cells decreases in magnitude rapidly as a denser mesh is used, up until roughly 300,000 elements, where the maximum temperature thereafter levels off and converges tightly toward an asymptote as the element number increases. For the HCD in Figure 5b, the same relationship applies, except with roughly 200,000 elements as the convergence point. This is why a mesh of 279,995 elements is to be used for the LCD model and 207,943 elements for the HCD since these accurately predict the thermal models for the LCD and HCD to a reasonable degree of scrutiny without the need for excessive computation time, especially in these cases where Fluent calculations can take upwards of 5 h to execute. However, it should be noted that the maximum temperatures at each of the mesh qualities tested in Figure 5a are extremely similar, with a total variation of only 0.0083% from the minimum density mesh to the maximum. The temperature reached the selected HCD mesh density (Figure 5b) at  $T_{\max} = 326.301$  K with 0.0032% error from the temperature recorded at 808,411 elements, which is also considered a precise enough result for this study.

### 3. Results

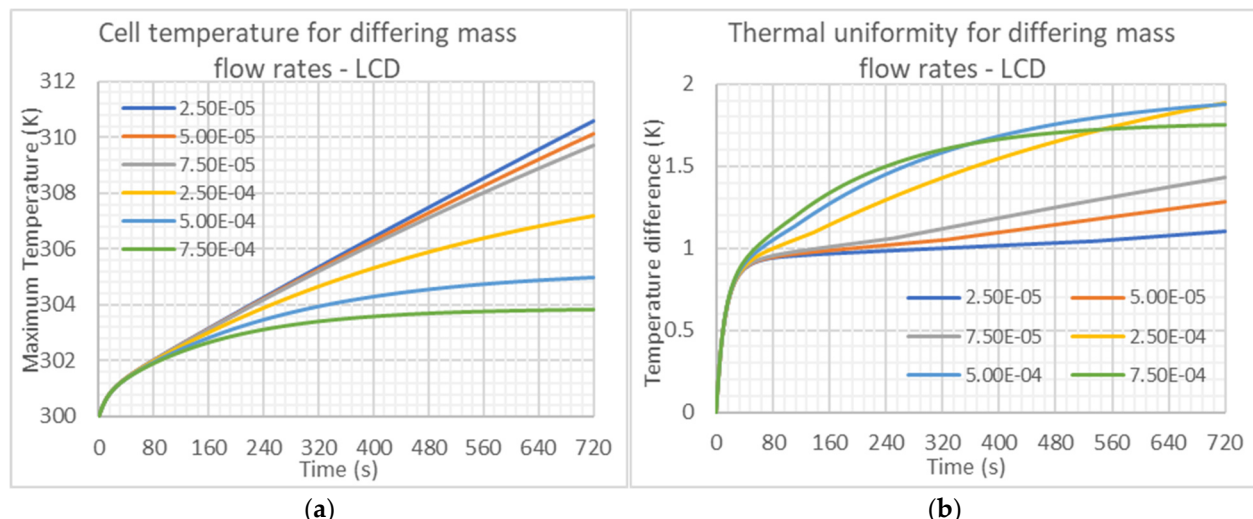
#### 3.1. Linear Channel (LCD) Results and Analysis

##### 3.1.1. Influence of Mass Flow Rate on the LCD

The first step of the design optimisation process for the LCD was to vary the inlet mass flow rate and examine the effect this has on the thermal performance of the battery pack. Six mass flow rates were tested, within the range of  $2.5\text{E-}05$  to  $7.5\text{E-}04 \text{ kg s}^{-1}$ , based on the range used by Yates et al. [45], and it should be noted that the three largest mass flow rates are an entire order of magnitude higher than the three lowest. This was done to achieve a wide range of results. The thermal performance was measured through the maximum temperature the lithium-ion cells would reach at each time step and the thermal uniformity of the cells (difference from minimum to maximum cell temperature at each time step) over the full 5C discharge cycle of 720 s. Table 3 shows a snapshot of the results taken at the 720th time step, after the discharge cycle concluded, and Figure 6a,b show the maximum temperature of the cells and the temperature difference in the cells, respectively.

**Table 3.** Influence of mass flow rate at 720 s-LCD.

Mass Flow Rate ( $\text{kg s}^{-1}$ )	$T_{\max}$ (K) at 720 s	$\Delta T$ (K) at 720 s
2.5E-05	310.595	1.105
5.0E-05	310.134	1.285
7.5E-05	309.695	1.431
2.5E-04	307.180	1.888
5.0E-04	305.004	1.881
7.5E-04	303.851	1.749

**Figure 6.** LCD-effects of mass flow rate on: (a) Maximum cell temperature; (b) Cell temperature difference.

A relationship can be seen from Figure 6a that as the inlet mass flow rate increases, the maximum temperature of the cells decreases. Within the first 80 s of the battery discharge, the temperatures recorded for each mass flow rate are very similar, and after this point, the temperatures deviate increasingly. This is due to the relationship of mass flow rate to the heat transfer coefficient and rate of heat flow, demonstrated in Equations (9) and (10), since the rate of heat flow varies linearly with mass flow rate. Figure 6b illustrates the thermal uniformity of the cells at each mass flow rate, wherein the first 40 s  $\Delta T$  increases rapidly. This is due to the surface of cells rapidly undergoing a change in temperature from the external liquid channel compared to the centre of the cells, creating a significant increase in temperature differential, for which the effects are gradually mitigated after 40 s as the core of the lithium-ion cells begin to cool at a similar rate to the surface. A temperature differential will be inevitably caused due to this being an indirect cooling method, where there are four liquid channels split evenly around each cell rather than each cell being evenly submerged in coolant liquid. Furthermore, with the LCD model, the central channel coolant will rise in temperature more rapidly than the other channels due to this channel being in closest proximity and equidistant from each cell. The channels on the corners will increase less in temperature due to being in proximity to only one cell. This is a limitation mainly induced by the size of the considered model, given it analyses only a sample of four cells from a full battery pack in order to not require unreasonable amounts of computational power to execute the Fluent calculation.

Interestingly in Figure 6b, it would seem that increasing the mass flow rate actually worsened the thermal uniformity of the battery pack, especially evident in the lowest three mass flow rates. This phenomenon was also documented in different cooling designs by Bai et al. [46] and Chen et al. [47]. The temperature difference for  $7.50\text{E-}04 \text{ kg s}^{-1}$  is the largest from 0–320 s, thereafter, it becomes lower than that of  $5.00\text{E-}04 \text{ kg s}^{-1}$  and then lower than that of  $2.50\text{E-}04 \text{ kg s}^{-1}$  after 530 s. This is likely due to the aforementioned phenomena where the surface of the cell is cooling rapidly compared to the core when the heat transfer

coefficient is higher due to the higher mass flow rate, and as the temperature regulates through the discharge cycle, this effect lessens since the rate of increase in temperature in the core begins to match that of the surface. Considering the optimal operating temperature for lithium-ion batteries lies between 298 K and 313 K [5] with a temperature difference of no greater than 5 K [5], the LCD battery pack immediately performed strongly in both regards, in that none of the mass flow rates tested resulted in results greater than these values (evident in Table 3). It is important to consider that using a high inlet mass flow rate in the cooling system inevitably draws more power, lowering the overall efficiency of the EV and potentially reducing its driving range. This is why although the concept of using the highest mass flow rate may be attractive, a compromise must be made to maintain higher efficiency in the EV. This is why the mass flow rate of  $7.50\text{E}-05 \text{ kg s}^{-1}$  has been chosen for further study, as it provides solid maximum temperature regulation ( $298 \text{ K} < T_{\max} < 313 \text{ K}$ ) and thermal uniformity ( $\Delta T < 5 \text{ K}$ ) whilst not requiring excessive power to run in an EV.

### 3.1.2. Influence of Linear Channel Diameter, $d_L$ , on the LCD

The next step of the design optimisation process for the LCD involved varying the diameter of the coolant channel, which would control the volume flow of fluid down the aluminium channels, and examine the effect this has on the thermal performance of the battery pack. Three values for channel diameter were tested, being  $d_L = 3 \text{ mm}$ ,  $6 \text{ mm}$  and  $9 \text{ mm}$ , illustrated in Figure 7a–c, respectively. In order to keep the simulations consistent, the total number of mesh elements for each simulation was kept as close as possible, despite the change in geometry. This was achieved through altering the body sizing of the aluminium channels, where the total mesh density was kept roughly between 277,000 and 281,000. The thermal performance was again measured through the maximum temperature reached by the cells for each time step and the temperature difference across the cells for each time step over the full 5C 720 s battery discharge cycle. Figure 8a,b show the maximum temperature of the cells and the temperature difference in the cells, respectively.

Figure 8a shows that as the diameter of the coolant channel increased, the maximum temperature of the lithium-ion cells decreased. This, however, was only over a small temperature range, taking the values at 720 s to be  $T_{\max} = 309.97 \text{ K}$  when  $d_L = 3 \text{ mm}$ , and  $T_{\max} = 309.31 \text{ K}$  at  $d_L = 9 \text{ mm}$ , indicating that the diameter of the coolant channels perhaps does not hold a large influence of the maximum temperatures, but still a noticeable one that is worth considering for optimisation. The study by Lai et al. [24], of a similar design to the LCD, only altered the diameter from 1–3 mm, providing a small range of results where a distinct relationship could not be found. The study performed in this paper, however, has used a significantly larger range of input parameters for diameter, where the relationship is well defined.

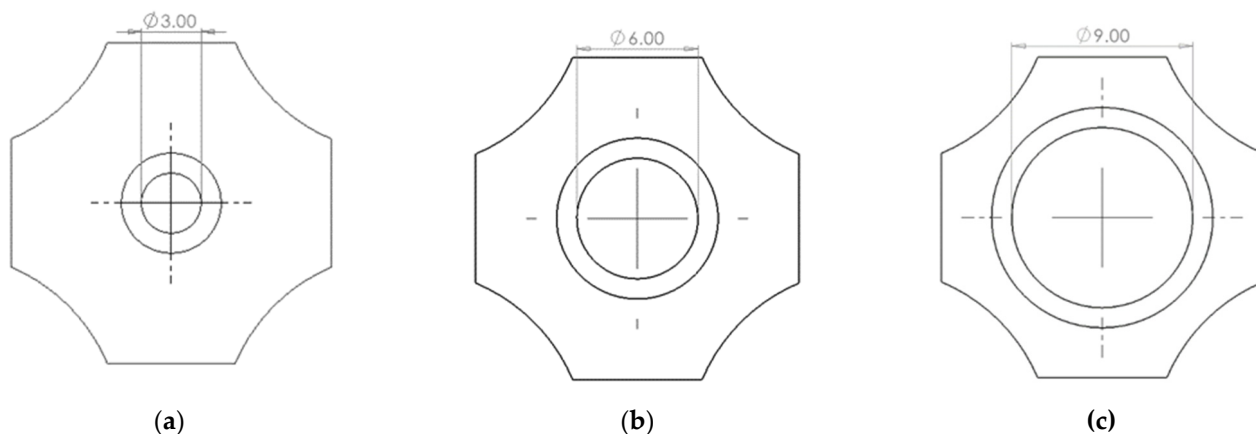


**Figure 7.** Top view of LCD channels for varying diameters: (a)  $d_L = 3 \text{ mm}$ ; (b)  $d_L = 6 \text{ mm}$ ; (c)  $d_L = 9 \text{ mm}$ .

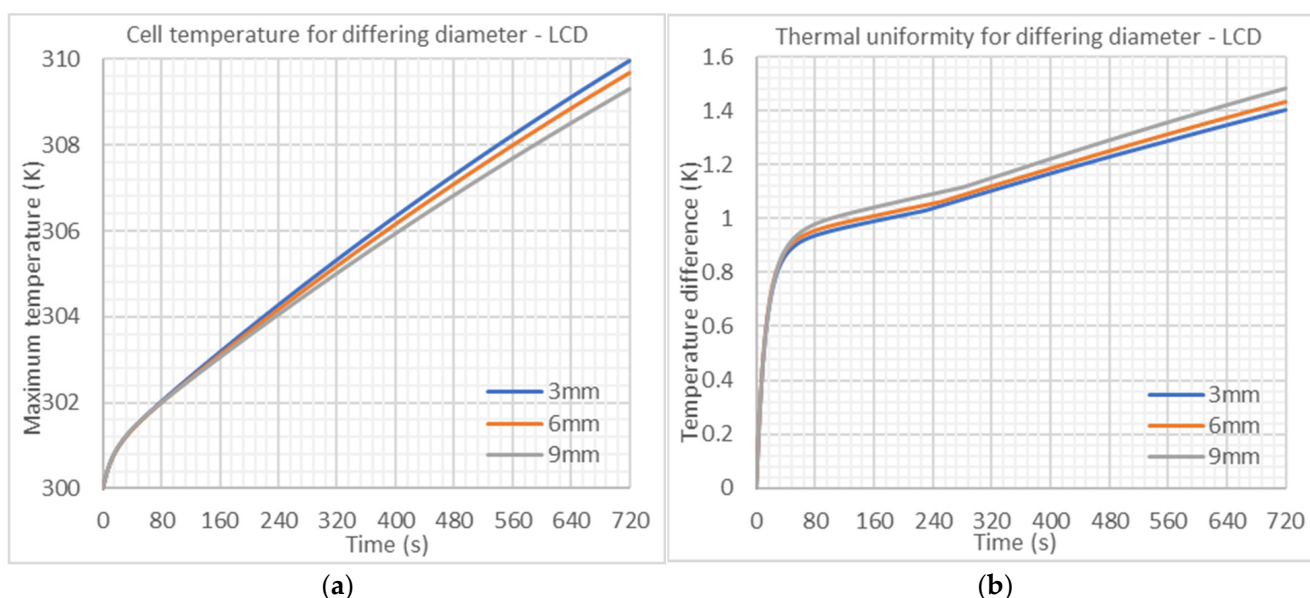


**Figure 8.** LCD—effects of channel diameter on: (a) Maximum cell temperature; (b) Cell temperature difference.

The relationship presented in Figure 8a is due to a combination of factors. On the one hand, since the inlet mass flow rate remains the same in each case but the fluid channel diameter is decreased (note the inlet in question is the inlet to the upper reservoir, for which the parameters are not changed), the water pressure and hence the fluid velocity is increased, which increases the heat transfer coefficient (see Equations (9) and (10)), providing increased levels of cooling to the lithium-ion cells. On the other hand, this effect is cancelled out by the fact that the heat transfer area between the fluid and the inside of the aluminium channel is decreased when the diameter is decreased. This results in a lower heat transfer (see Equation (10)) which leads to reducing the cooling capability. From these results, evidently, the latter effect has a slightly larger influence over the maximum cell temperature compared to the former effect, but the cancellation is also still evident in that  $T_{\max}$  only has a maximum variance of 0.66 K across the smallest and largest diameter tested.

Figure 8b shows that as the channel diameter increases, the thermal uniformity worsens, but only marginally. At the end of the 5 C discharge cycle ( $t = 720$  s),  $\Delta T = 1.404$  K when  $d_L = 3$  mm and  $\Delta T = 1.408$  K when  $d_L = 9$  mm, which is a very small range of temperature difference and is due to the same aforementioned reasoning for the results in Figure 8a. Both the maximum cell temperature and thermal uniformity are kept within the optimal range of  $298 \text{ K} < T_{\max} < 313 \text{ K}$  and  $\Delta T < 5 \text{ K}$  for all diameters, although since the maximum temperature reduction is more apparent for the  $d_L = 9$  mm case in relation to the worsening of thermal uniformity, and also since  $T_{\max}$  values are closer to the upper boundary of 313 K, the 9 mm diameter channel geometry is selected as most optimal and will be considered for further study.

### 3.1.3. Influence of Inlet and Outlet Locations on the LCD

Based on the methods of Yates et al. [45], the final optimisation step for the LCD involved varying the locations of the fluid domain inlets and outlets and examining the effect this has on the thermal performance of the battery pack. Five different combinations of locations were tested, for which the locations are presented in diagram form in Figure 9 and the combinations of these locations are presented in Table 4.

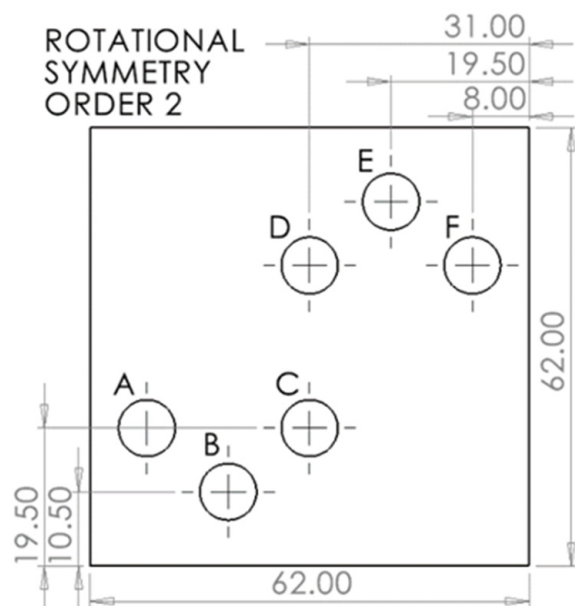


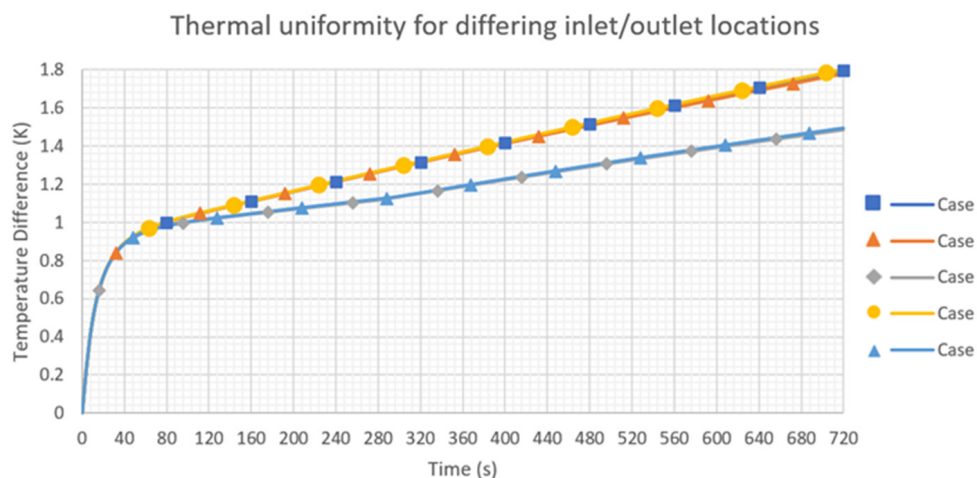
**Figure 9.** Inlets (A–C) and outlets (D–F) locations (dimensions in mm)–LCD.

**Table 4.** Thermal performance of location combinations at  $t = 720$  s–LCD.

Location Combination	$T_{\max}$ (K) at 720 s	$\Delta T$ (K) at 720 s
Case 1 = A, F	309.366	1.796
Case 2 = B, E	309.362	1.779
Case 3 = C, D	309.308	1.484
Case 4 = A, D	309.364	1.799
Case 5 = C, F	309.321	1.492

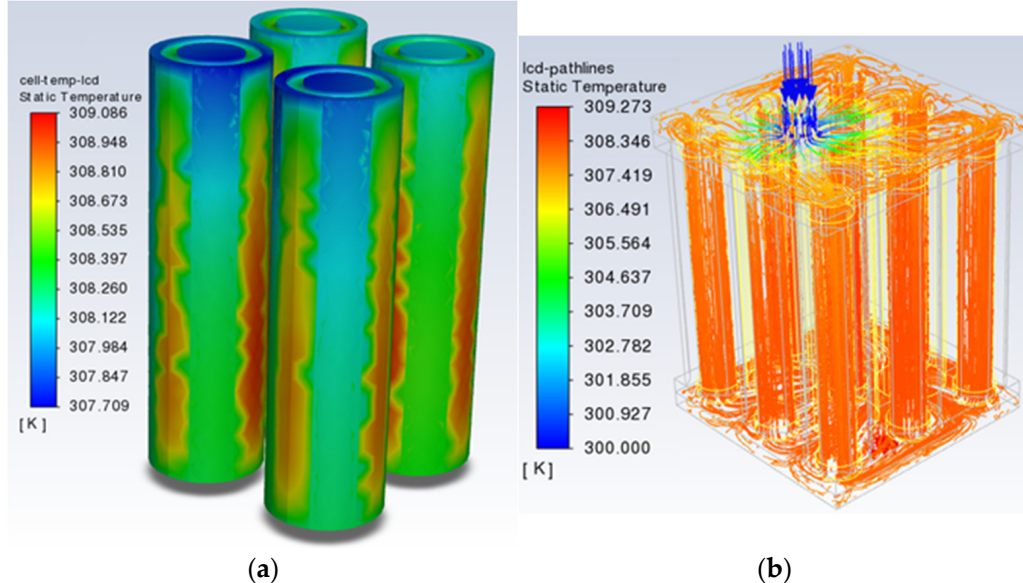
When selecting the locations, it was important to make sure that the inlet was not directly above one of the aluminium channels since, in reality, the coolant would not be able to spread evenly in the upper reservoir to flow through each channel. The metrics used for assessing the thermal performance of the battery pack were again the maximum temperature reached in the lithium-ion cells and the temperature difference across the cells over the full 5C 720 s battery discharge cycle. Table 4 shows the maximum temperature and temperature difference measured at the 720th time step (end of the discharge cycle), and Figure 10 shows the temperature difference in the cells. The main objective of this stage was to optimise thermal uniformity since only location conditions are being altered, which will not have a significant impact on the maximum temperature reached. This is why the graph for maximum temperature is not plotted, as the curves for each combination are more or less on top of each other, providing little analytical benefit.

Figure 10 shows the results of the five combination cases applied in this study, where line markers were applied for clarity. Cases 3 and 5 performed the strongest in terms of thermal uniformity, whereas cases 1, 2 and 4 were lacking in comparison. Cases 3 and 5 both used location C as an inlet (see Table 4 and Figure 9), and as this is the common factor, it is most likely the reason for higher performance in these cases. This is because location C provided the most central location out of all the inlets in relation to the LCD battery pack, providing the most even distribution of coolant to all of the lithium-ion cells. This data also shows that the location of the inlet holds greater significance to the thermal performance than the location of the outlet since using outlets D and F in cases 3 and 5, respectively, gave very similar results, as shown in Figure 10 and Table 4.



**Figure 10.** Cell temperature difference over discharge cycle for differing inlet/outlet locations—LCD.

All of the inlet and outlet combinations tested fell well within the optimal temperature regions of  $298 \text{ K} < T_{\max} < 313 \text{ K}$  and  $\Delta T < 5 \text{ K}$ . Although the results in Table 4 show that case 3 provided the best results in both regards, with  $T_{\max} = 309.308 \text{ K}$  and  $\Delta T = 1.484 \text{ K}$  at the conclusion of the discharge cycle, just slightly ahead of case 5 in performance. The LCD battery pack is now considered optimised within the bounds of this research, using inlet location C and outlet location D (Figure 10). The final temperature contours for the LCD are shown in Figure 11, whereas in Figure 11a, the effects of the aluminium channel contact area are evident in the lower temperature regions.



**Figure 11.** LCD contours: (a) Cell temperature (K); (b) Fluid pathlines.

An experimental case was conducted by Sheng et al. [25] with the cellular liquid cooling jacket containing liquid channels running parallel to the battery length, similar in design to this study. Using cylindrical 21,700 Li-ion cells operating at 2.5C discharge rate, the maximum cell temperature reached was 312 K, just falling under the upper boundary in the optimal region of  $298 \text{ K} < T_{\max} < 313 \text{ K}$ , in similar fashion to the LCD, having a  $T_{\max}$  value just below at 309.308 K. The maximum temperature difference in this case found by Sheng et al. was approximately  $\Delta T = 1.4 \text{ K}$ , extremely close to the  $\Delta T = 1.484 \text{ K}$  achieved by the LCD, validating this study's results.

### 3.2. Helical Channel Design (HCD) Results and Analysis

#### 3.2.1. Influence of Mass Flow Rate on the HCD

The inlet mass flow rate of coolant must be optimised for the HCD in order to contribute to the objectives of maximum temperature regulation of  $298 \text{ K} < T_{\max} < 313 \text{ K}$  and thermal uniformity of  $\Delta T < 5 \text{ K}$  whilst remaining realistic for the use in an electric vehicle. Six mass flow rates were tested in the range of  $2.50\text{E}-05$  to  $7.50\text{E}-04 \text{ kg s}^{-1}$ . Table 5 shows a snapshot of the results taken at the 720th time step (after the discharge cycle has concluded). Figure 12a,b show the maximum temperature of the cells and the temperature difference in the cells across the entire discharge cycle, respectively.

**Table 5.** Influence of mass flow rate at 720 s–HCD.

Mass Flow Rate ( $\text{kg s}^{-1}$ )	$T_{\max}$ (K) at 720 s	$\Delta T$ (K) at 720 s
$2.50\text{E}-05$	326.301	16.462
$5.00\text{E}-05$	324.562	19.332
$7.50\text{E}-05$	322.081	18.964
$1.00\text{E}-04$	319.264	17.197
$2.00\text{E}-04$	311.201	10.396
$7.50\text{E}-04$	303.702	3.439

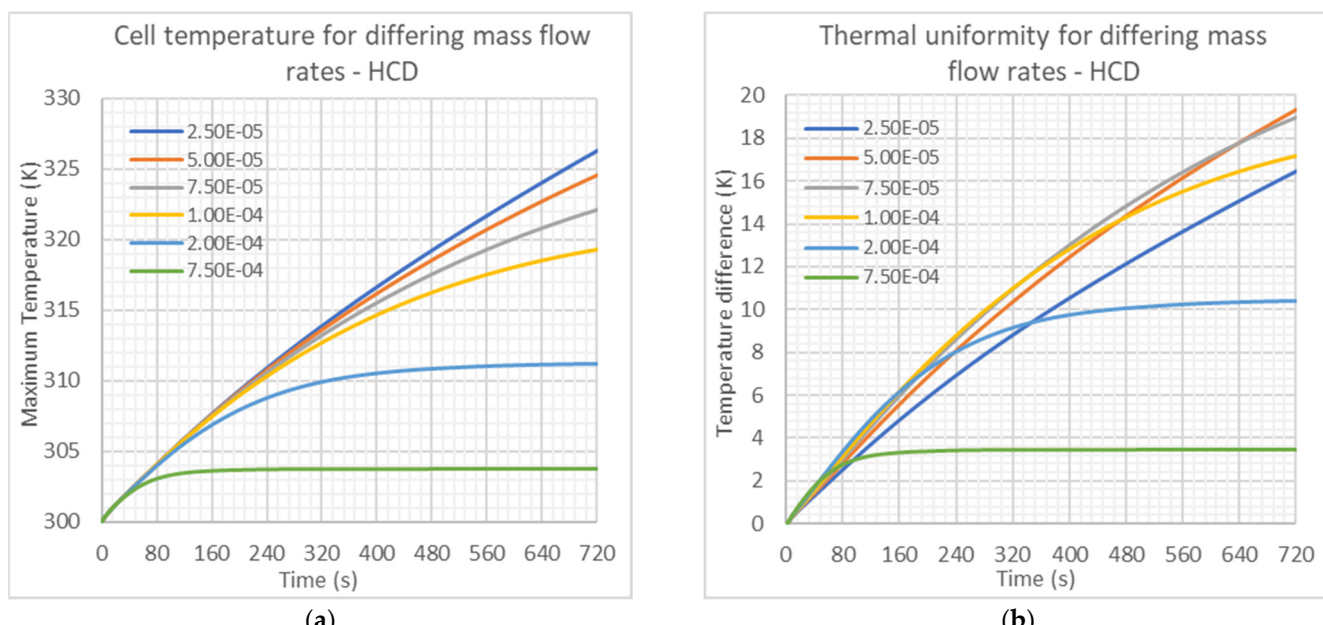


**Figure 12.** HCD–effects of mass flow rate on: (a) Maximum cell temperature; (b) Cell temperature difference.

As can be seen in Figure 12a, the same relationship as in the LCD (Figure 6b) can be found where as the mass flow rate increases, the maximum cell temperature decreases. The same explanation of this relationship as given for the LCD can also be applied here, where the link of mass flow rate to heat transfer coefficient given in Equations (9) and (10) provides increased cooling capability with a higher mass flow rate. Figure 12b shows the thermal uniformity in the form of temperature difference in the cells, where the relationship with mass flow rate is unclear. In general, thermal uniformity is improving with higher mass flow rates. Although the test with  $2.50\text{E}-05 \text{ kg s}^{-1}$  seems to not align with this trend, as it exhibits a lower temperature difference than with the  $5.00\text{E}-05 \text{ kg s}^{-1}$ ,  $7.50\text{E}-05 \text{ kg s}^{-1}$  and  $1.00\text{E}-04 \text{ kg s}^{-1}$  mass flow rates. Additionally, the temperature difference over the full 720 s discharge cycle for the  $5.00\text{E}-05 \text{ kg s}^{-1}$ ,  $7.50\text{E}-05 \text{ kg s}^{-1}$  and  $1.00\text{E}-04 \text{ kg s}^{-1}$  mass flow rates seem to overlap each other at varying points in the cycle. These occurrences were

also reported by Zhou et al. [21] in a similar study and can be accounted for simply by a computational error.

The results of the HCD immediately seem to give the impression of a lack of performance relative to the LCD. The maximum temperatures reached for the HCD (Table 5) are much higher for the same mass flow rates used as the LCD (Table 3). For example, where both designs used  $m = 2.50E-05 \text{ kgs}^{-1}$ , the LCD gave  $T_{\max} = 310.595 \text{ K}$ , but the HCD gives  $T_{\max} = 326.301 \text{ K}$ , an increase in temperature by  $15.706 \text{ K}$ , and well beyond the desired value within  $298 \text{ K} < T_{\max} < 313 \text{ K}$ . The thermal uniformity of the lithium-ion cells in the HCD has also worsened in comparison to the LCD, wherein the LCD  $\Delta T$  remained between  $1.105 \text{ K}$  and  $1.888 \text{ K}$  (Table 3) for all tested mass flow rates. However, the HCD reached its highest temperature difference of  $19.332 \text{ K}$  at  $m = 5.00E-05 \text{ kgs}^{-1}$ . This can be due to a multitude of reasons, one being the lessened contact area with aluminium acting as a heat sink for the HCD, meaning the rate of heat dissipation through the aluminium channel will be lessened. Furthermore, the coolant within the helical channels is inevitably in closer proximity to the cells due to the channels needing to weave in complete circumference to the batteries. This includes the points where the distance between each cylindrical battery is a minimum, rather than with the LCD where the centroid of a coolant channel is always at the point of maximum distance in-between each cell. This means that the top of the cells (positive electrode) will be cooled at a higher rate, with the coolant fluid increasing in temperature more rapidly as it reaches the bottom (negative electrode), creating a more significant imbalance in temperature throughout each cell.

Since the mass flow rates of  $2.50E-05 \text{ kgs}^{-1}$  to  $1.00E-04 \text{ kgs}^{-1}$  resulted in a higher temperature than the objective of  $298 \text{ K} < T_{\max} < 313 \text{ K}$  evident in Table 5, they have been automatically rejected, and the temperature difference also lies above the goal of  $\Delta T < 5 \text{ K}$ . A mass flow rate of  $2.00E-04 \text{ kgs}^{-1}$  was selected for further study, given this is the lowest tested mass flow rate for  $T_{\max}$  to fall below  $313 \text{ K}$ , providing  $T_{\max} = 311.201 \text{ K}$  and  $\Delta T = 10.396 \text{ K}$ . Although  $\Delta T$  remains above the desired  $5 \text{ K}$ , further optimisation to the geometry of the HCD shall be carried out to reduce this. Additionally, the selected mass flow rate should not be too high as this requires more power to operate within an EV, reducing the overall efficiency and driving range. This means the HCD is already at a disadvantage compared to the LCD since a higher mass flow rate must be used in order to keep  $T_{\max}$  within acceptable levels.

### 3.2.2. Influence of Helical Channel Diameter, $d_H$ , on the HCD

The next chosen design optimisation for the HCD involved altering the diameter of the helical coolant channels in order to examine and evaluate the effect this has on the thermal performance of the battery pack. Four values for diameter were tested, comprising  $d_H = 2 \text{ mm}$ ,  $3 \text{ mm}$ ,  $4 \text{ mm}$ , and  $5 \text{ mm}$ , illustrated in Figure 13, where the total height of each helix and the dimensions of the reservoirs were altered slightly each time to keep the structure consistent. Due to the nature of the helical geometry, the diameters, unfortunately, cannot be increased beyond  $5 \text{ mm}$ , since the channels would be in contact with each other at the point of closest proximity between the batteries, which provides another limitation in comparison to the LCD. The drawings shown in Figure 13 are cross-section views of the helical channel, where the channel would be in contact with the battery along the flat edge. Once again, to keep the simulations consistent, the total number of mesh elements for each case was kept between 207,212 and 207,943 by altering the body sizing of the channel since this mesh density was considered accurate from the HCD mesh dependency study. Figure 14a,b show the maximum temperature and temperature difference, respectively, achieved in the full 5C 720 s discharge cycle.

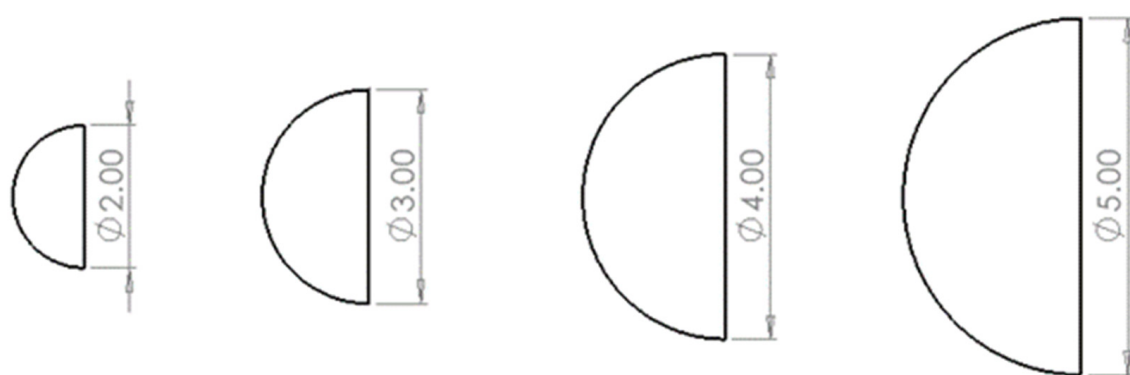


**Figure 13.** Varying diameter for HCD channels—cross-section view (dimensions in mm).

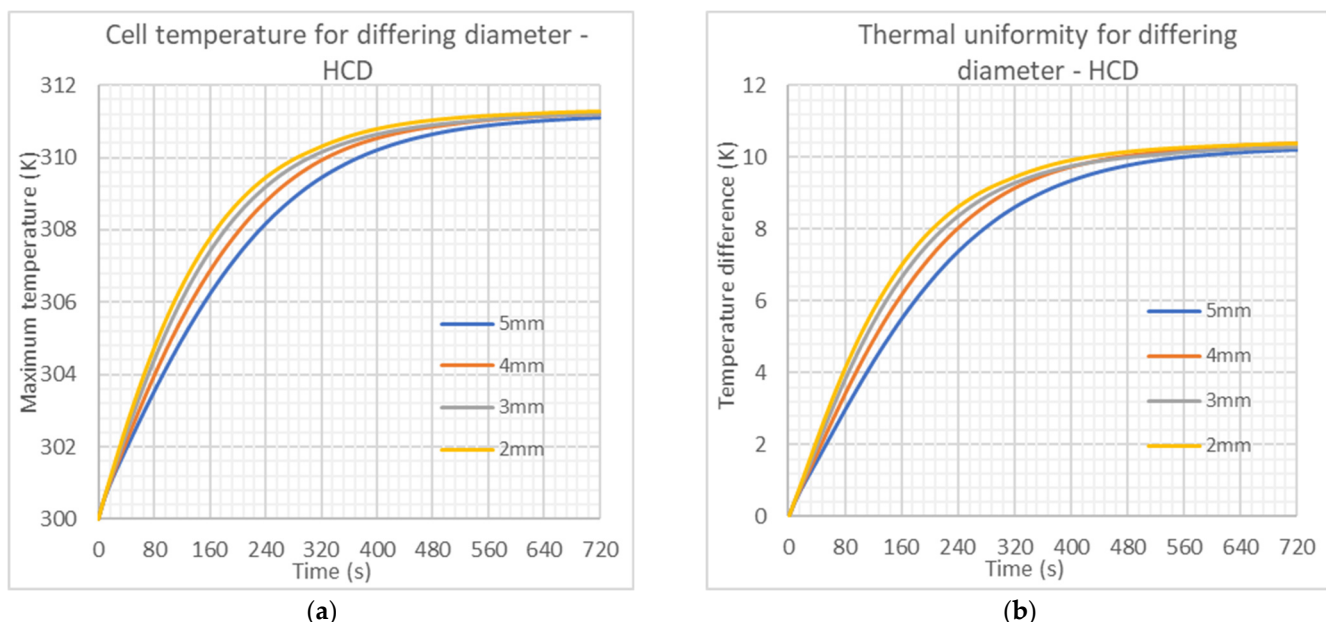


**Figure 14.** HCD—effects of channel diameter on: (a) Maximum cell temperature; (b) Cell temperature difference.

Figure 14a,b both show a very similar relationship in the characteristics of each tested diameter over the 720 s discharge cycle. From roughly 5% DOD ( $t = 40$  s) to 60% DOD ( $t = 440$  s), the difference in performance for each diameter is most noticeable, where the larger diameter channel performs better in terms of maximum temperature reduction and thermal uniformity. Beyond this point, up until the conclusion of the discharge cycle, the performance difference of each diameter is less apparent but still follows the aforementioned relationship. These results follow a similar relationship to the findings of the double helix structure proposed by Dong et al. [22], although a larger range of diameters has been tested within this research compared to Dong et al. [22] and the half helical design proposed by Zhou et al. [21], in order to fully define the relationship between channel diameter and thermal performance. In a similar fashion to the LCD channel diameter test, the larger helical diameters for HCD provide stronger overall cooling due to the increased contact surface area with the lithium-ion cells, which in turn increases the heat transfer rate (described in Equation (10)).

At  $t = 720$  s, when  $d_H = 5$  mm the value of  $T_{\max} = 311.104$  K and  $\Delta T = 10.224$  K, whereas when  $d_H = 2$  mm the value of  $T_{\max} = 311.282$  K and  $\Delta T = 10.384$  K. This shows that the increase in diameter reduced maximum temperatures by 0.178 K and improved thermal uniformity by 0.16 K. Although this is not a significant amount, it is still worth considering,

especially when the values of  $T_{\max}$  and  $\Delta T$  were improved by up to approximately 1 K at the earlier DOD, which in the long term will mitigate the de-ageing of the lithium-ion cells [5]. This is why the 5 mm diameter for the helical channels is to be selected as optimal. At this stage, the maximum temperature is within the objective region of  $298 \text{ K} < T_{\max} < 313 \text{ K}$ , but unfortunately, the thermal uniformity could not be reduced to the desired  $\Delta T < 5 \text{ K}$ , which will be attempted during the final stage of optimisation.

### 3.2.3. Influence of Inlet and Outlet Locations on the LCD

The final stage of optimisation for the HCD involved altering the inlet and outlet locations for the fluid domain and examining the effect this has on the thermal performance of the battery pack. Three combinations of inlet/outlet locations were tested, where the locations are mapped in Figure 15, and the combinations are noted in Table 6. The central hole shown in Figure 15 is named by both I (inlet) and J (outlet) since they overlap in the top view, the inlet is on the upper reservoir, and the outlet is on the lower reservoir.

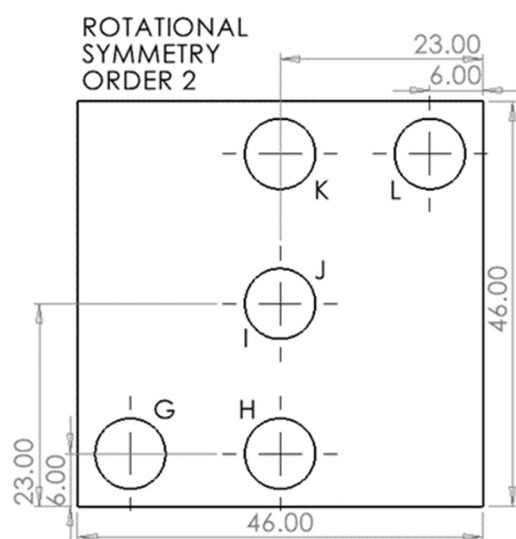


**Figure 15.** Inlets (G–I) and outlets (J–L) locations (dimensions in mm)—HCD.

**Table 6.** Thermal performance of location combinations at  $t = 720 \text{ s}$ —HCD.

Location Combination	$T_{\max}$ (K) at 720 s	$\Delta T$ (K) at 720 s
Case 1 = G, L	311.279	10.794
Case 2 = I, J	311.104	10.224
Case 3 = H, K	311.328	10.733

It was established for the LCD that the combinations that were not symmetrical in both axes performed weakest and that the inlet location is the dominant factor compared to the outlet location, so in this study, only the three cases need to be analysed. For each tested combination, the values for  $T_{\max}$  and  $\Delta T$  at 720 s are presented in Table 6, along with the temperature difference graph shown in Figure 16 representing thermal uniformity.

Figure 16 shows the results of the three combinations, where it is conclusive that Case 2 has performed the strongest in terms of improving thermal uniformity, making use of inlet I and outlet J (see Figure 15). This is due to this inlet and outlet providing the most central location of all the possibilities, ensuring an even distribution of coolant for the lithium-ion cells. All the combinations tested provided maximum temperatures within the goal of  $298 \text{ K} < T_{\max} < 313 \text{ K}$ , however, the thermal uniformity still could not be reduced down to  $\Delta T < 5 \text{ K}$  for the HCD, although Case 2 did get the closest to reaching this goal, with a value for  $T_{\max} = 311.104 \text{ K}$  and  $\Delta T = 10.224 \text{ K}$ . Figure 17 shows the final temperature contours for the HCD.

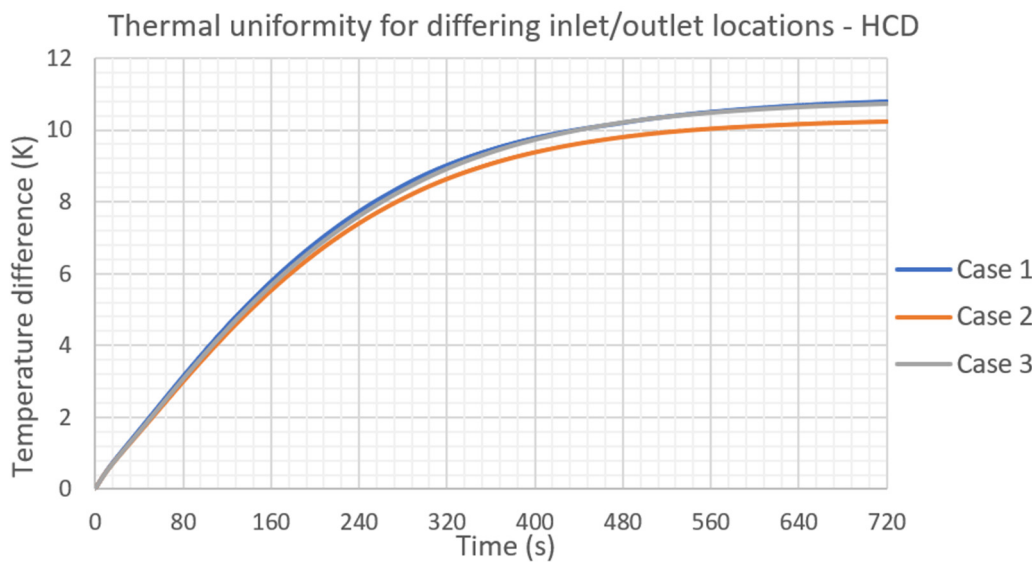


**Figure 16.** Cell temperature difference over discharge cycle for differing inlet/outlet locations–HCD.

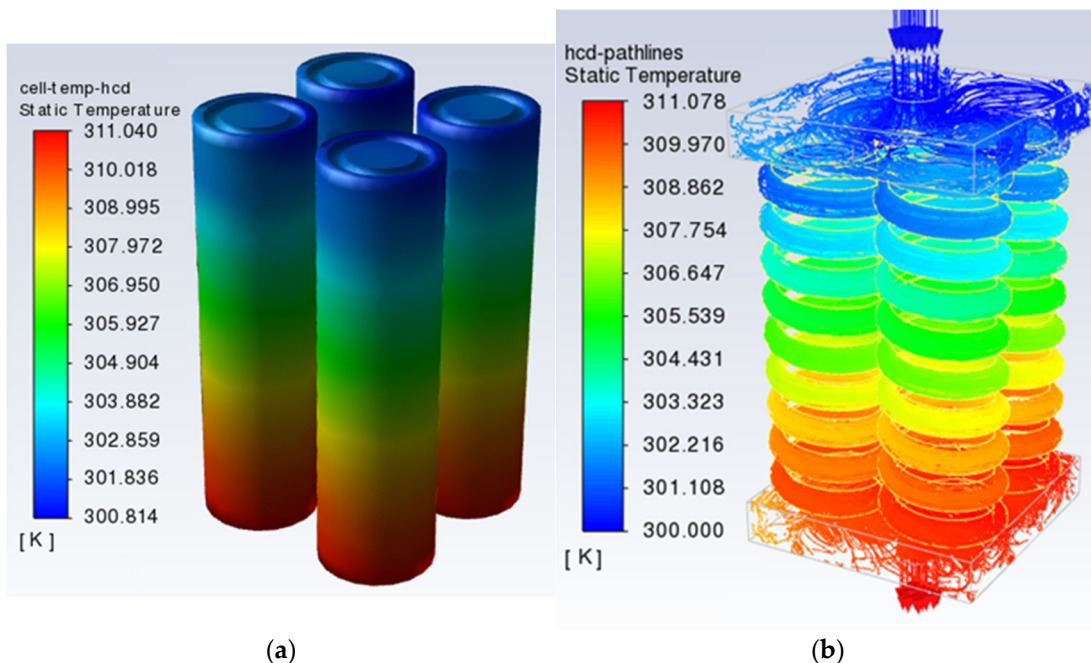


**Figure 17.** HCD contours: (a) Cell temperature (K); (b) Fluid pathlines.

In terms of experimental validation, a double helix cooling plate with PCM cooling for 18,650 cylindrical cells was investigated by Yu et al. [7], achieving maximum temperatures varying between  $310 \text{ K} < T_{\max} < 313 \text{ K}$ , where the HCD in this study achieves a similar result of 311.104 K. The CFD simulations conducted in the literature on helical duct liquid cooling structures similar to the HCD also seem to have issues with regulating temperature difference. Dong et al. [22] achieved  $\Delta T = 7.01 \text{ K}$  after the use of optimisation algorithms for the double helix structure, and Zhou et al. [34] achieved  $\Delta T = 6.7 \text{ K}$  for the half-helical duct structure, both falling outside the optimal range of  $\Delta T < 5 \text{ K}$ .

### 3.3. Comparison of the LCD and HCD

The fully optimised LCD and HCD structures illustrated in Figure 18a,b, respectively, shall now be compared and evaluated. Figures 19 and 20 show the maximum temperatures reached and the temperature difference in the lithium-ion cells, respectively, over the same

5C 720 s discharge. The LCD clearly provides a superior cooling performance compared to the HCD in both metrics, where  $T_{\max} = 309.308$  K and  $\Delta T = 1.484$  K at 720 s, compared to that of  $T_{\max} = 311.104$  K and  $\Delta T = 10.224$  K reached by the cells in the HCD, a reduction of 1.796 K in maximum temperature and 8.740 K in temperature difference. This is on top of the fact that the LCD could make use of a lower value for inlet mass flow rate, providing a lower power consumption requirement to run the thermal management system, maximising the efficiency of the given EV.

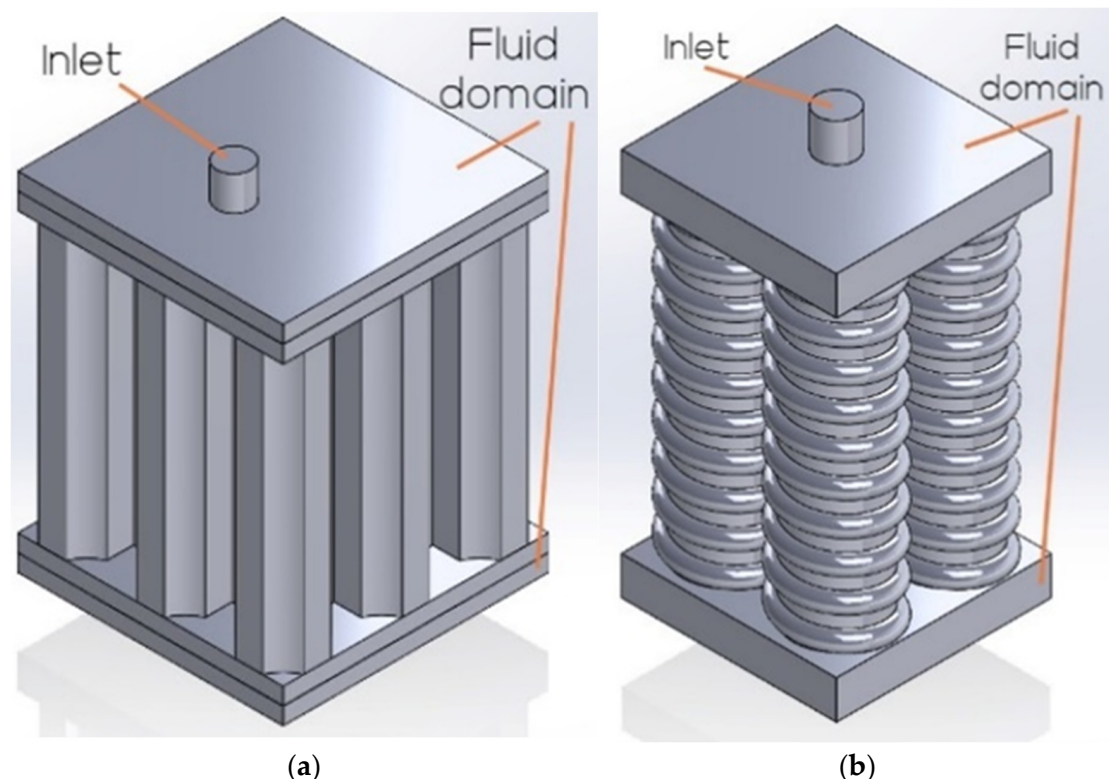


**Figure 18.** ISO views for the final optimised battery packs: (a) LCD; (b) HCD.

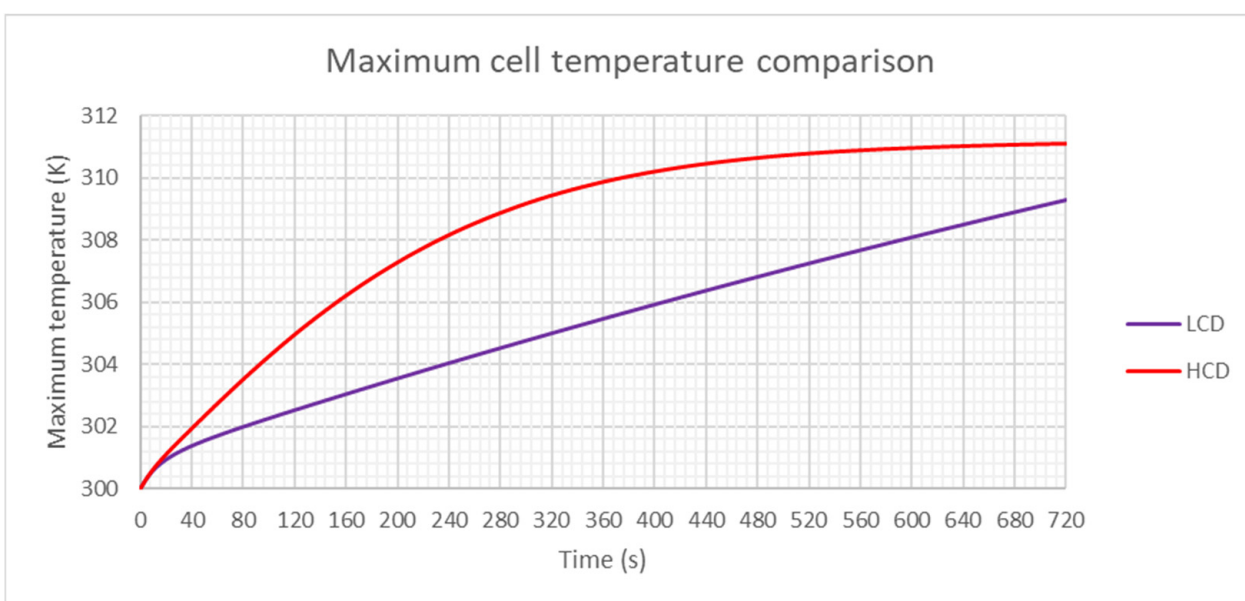


**Figure 19.** Maximum cell temperature comparison—LCD & HCD.

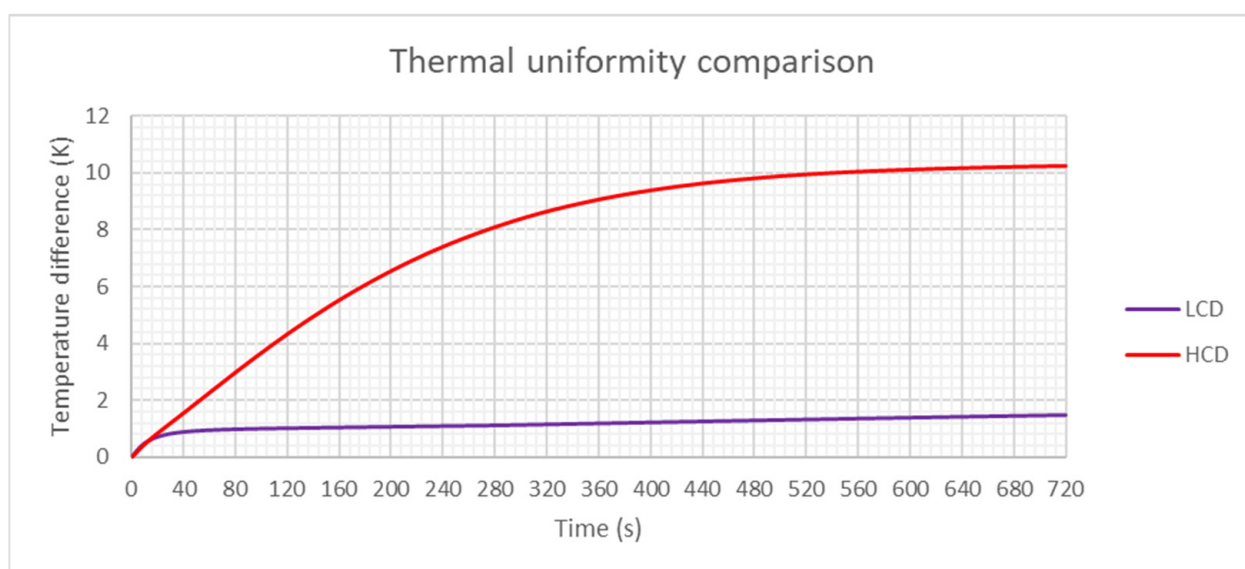


**Figure 20.** Cell temperature difference comparison—LCD & HCD.

Both objectives of  $298 \text{ K} < T_{\max} < 313 \text{ K}$  and  $\Delta T < 5 \text{ K}$  were achieved for the LCD comfortably, and the maximum temperature objective for the HCD was also achieved, albeit slightly higher in magnitude compared to the LCD. However, the objective to control temperature difference under 5 K was not achieved by the final HCD structure. Theoretically, the objective could be achieved by using a higher mass flow rate, as shown in Table 5. Although this would have to compromise even further on the overall efficiency of the EV, given its requirement of much higher power consumption, preventing this power from being more usefully allocated to other systems in the EV.

Excluding the masses of the lithium-ion cells, the mass of the HCD structure comes to 50.2 g, and the mass of the LCD comes to 285 g, given the volumes computed from SolidWorks 2021 and the mass density of aluminium to be  $2719 \text{ kgm}^{-3}$  from Table 2. This at least gives the HCD the advantage of being much more lightweight, which is a quality that vehicle manufacturers will strive for to achieve maximal efficiency. Given that the cells are arranged in the same spacing for both designs and both designs output the same power (but at different temperatures), the volumetric energy densities are the same for each design when considering a full EV battery pack. The HCD has a 5.7 times higher gravimetric energy density, based on the ratio of weights for each design. From a manufacturing standpoint, the helical channels could be made in a similar fashion to a compression spring using a CNC spring coiler machine, followed by heat treatment and grinding. Although it would need to be heat treated and moulded awkwardly to shell out the pipe providing the medium for fluid flow. This would be a significantly more complicated manufacturing process than that of the linear channels, whereby, for example, a drill press could be used for the extruded cut. This also would lead to the LCD being cheaper to manufacture and simpler to maintain and clean, given there is less need for specialised equipment to clean a straight pipe compared to a helical pipe.

The LCD would prove to be a more applicable thermal management system for use in electric vehicles given its lower power consumption, and overall superior cooling effectiveness compared to the HCD. The LCD could also be adapted to large scale energy storage applications due to the simplicity of its manufacturing, meaning high volumes for a large battery pack would be more economical to produce.

The shortfalls of the HCD are mainly due to the lack of significant contact area for a heatsink and the lack of aluminium. This is corroborated by the designs tested by Yates et al. [45], where the use of a heat sink in one design provided better thermal uniformity compared to one without. Additionally, due to the closer proximity of the coolant

to the cells in the HCD, an imbalance in temperature is created from the top of the cells (positive electrode) to the bottom (negative electrode).

#### 4. Discussion and Conclusions

In this research, two liquid cooling structures for EV lithium-ion battery packs, denoted as the LCD and HCD, were designed and evaluated. The heat generation of a 18,650 cell undergoing a 5C discharge cycle was modelled with the standardised 300 K inlet temperature for the coolant water. The thermal performance of the cells were analysed throughout the discharge cycle. Each design underwent a series of numerical and geometrical optimisations, comprising the variance of inlet mass flow rate, channel diameter and inlet and outlet locations. The metrics used for measuring the thermal performance were the maximum temperature and temperature difference (thermal uniformity). The important findings are as follows:

- The performance of each design, especially the HCD, was most significantly dependent on the inlet mass flow rate. It was found that as mass flow rate increases, the maximum cell temperature decreases due to the relationship between flow velocity and the heat transfer coefficient. The thermal uniformity improved for the HCD, and thermal uniformity worsened for the LCD, with a few discrepancies.
- As the channel diameter increased for each design, the maximum temperature decreased due to the relationship between contact area and heat transfer rate. The thermal uniformity for the HCD improved, whereas it worsened slightly for the LCD. The improvement in temperature regulation was more apparent towards the end of the discharge cycle for the LCD, but for the HCD, it was more apparent during the 5% to 60% DOD range.
- The thermal uniformity was optimal when the inlet and outlet were centralised, providing the evenest distribution of coolant among the four cells. Additionally, the location of the inlet was more significant in influencing the thermal performance than the location of the outlet.
- The optimal LCD provided a cell  $T_{\max}$  of 309.308 K and  $\Delta T$  of 1.484 K at  $t = 720$ s, well within the objectives of  $298 \text{ K} < T_{\max} < 313 \text{ K}$  and  $\Delta T < 5 \text{ K}$ . The final design used a mass flow rate of  $7.50\text{E-}05 \text{ kgs}^{-1}$ , channel diameter of 9 mm and manifold locations C & D (see Figure 10).
- The optimal HCD provided a cell  $T_{\max}$  of 311.104 K and  $\Delta T$  of 10.224 K at  $t = 720$  s, meeting the objective of  $298 \text{ K} < T_{\max} < 313 \text{ K}$  but failing to satisfy  $\Delta T < 5 \text{ K}$ . The HCD could have theoretically reached the  $\Delta T$  objective by using a higher inlet mass flow rate, but in the interest of keeping the design realistic for use in an EV, the mass flow rate was limited. The final design used a mass flow rate of  $2.00\text{E-}04 \text{ kgs}^{-1}$ , channel diameter of 5 mm and manifold locations I & J (see Figure 15).
- The LCD provided much stronger results than the HCD, even while making use of a lower mass flow rate, reducing the power draw for the cooling system to operate. The LCD is also simpler to manufacture, although it does weigh more, potentially harming the overall efficiency and the driving range of the EV in question.

Some limitations of this study include that the material properties for the battery were generalised and that the heat generation model was assumed to be uniform throughout the volume of the battery, along with not being a function of time or temperature. Due to the nature of the cooling system geometry, the cylindrical cells could not be structured in a staggered layout, which would be more compact and applicable in the design of EVs. Furthermore, only four lithium-ion cells were modelled in this battery pack simulation in order to mitigate unnecessarily high computational requirements. Future work could therefore evaluate these models on a larger scale more accurate to a real EV battery pack. Additionally, analysing different materials for the cooling structure other than aluminium as well as different coolants such as various glycol aqueous solutions would be useful to optimise these designs further. It is also recommended that experimental studies are conducted in future research for helical type channel designs similar to the HCD, as currently

very little data exists for structures similar to this. Finally, the MSMD battery model within Fluent could be used to develop a more accurate heat generation model providing more applicable results, although requiring a slight reconstruction of some geometries.

**Author Contributions:** Conceptualization, R.L. and M.A.; methodology, R.L. and M.A.; software, R.L. and M.A.; validation, R.L. and M.A.; formal analysis, R.L. and M.A.; investigation, R.L. and M.A.; resources, M.A.; data curation, R.L.; writing—original draft preparation, R.L.; writing—review and editing, M.A.; visualization, R.L. and M.A.; supervision, M.A.; project administration, M.A. All authors have read and agreed to the published version of the manuscript.

**Funding:** This research received no external funding.

**Institutional Review Board Statement:** Not applicable.

**Informed Consent Statement:** Not applicable.

**Data Availability Statement:** Not applicable.

**Conflicts of Interest:** The authors declare no conflict of interest.

## Nomenclature

Variables			
A	contact area ( $\text{m}^2$ )	HCD	electric vehicle
c	specific heat capacity ( $\text{Jkg}^{-1} \text{K}^{-1}$ )	LCD	helical channel design
d	channel diameter (mm)	MSMD	linear channel design
h	heat transfer coefficient ( $\text{Wm}^{-2} \text{K}^{-1}$ )	PCM	multi-scale multi-domain
I	current (A)	SOC	phase change material
k	thermal conductivity ( $\text{Wm}^{-1} \text{K}^{-1}$ )		state of charge
L	characteristic length (m)	Greek letters	
m	mass (kg)	$\Delta$	
$\dot{m}$	mass flow rate ( $\text{kgs}^{-1}$ )	$\mu$	difference
P	pressure (Pa)	$\rho$	dynamic viscosity ( $\text{kgm}^{-1} \text{s}^{-1}$ )
q	heat generation ( $\text{Wm}^{-3}$ )		mass density ( $\text{kgm}^{-3}$ )
Q	rate of heat flow (W)	Subscripts	
R	resistance ( $\Omega$ )	b	battery
Re	Reynolds number	gen	generation
T	temperature (K)	H	helical
t	time (s)	L	linear
U	open-circuit voltage (V)	max	maximum
V	volume ( $\text{m}^3$ )	p	constant pressure process
v	velocity ( $\text{ms}^{-1}$ )	w	water
Acronyms			
CAD	computer-aided design		
CFD	computational fluid dynamics		
DOD	depth of discharge		

## References

1. Navas-Anguita, Z.; García-Gusano, D.; Iribarren, D. A review of techno-economic data for road transportation fuels. *Renew. Sustain. Energy Rev.* **2019**, *112*, 11–26. [[CrossRef](#)]
2. COP26 Declaration on Accelerating the Transition to 100% Zero Emission Cars and Vans. Available online: <https://www.gov.uk/government/publications/cop26-declaration-zero-emission-cars-and-vans/cop26-declaration-on-accelerating-the-transition-to-100-zero-emission-cars-and-vans> (accessed on 4 August 2022).
3. Liu, Y.; Zhang, R.; Wang, J.; Wang, Y. Current and future lithium-ion battery manufacturing. *iScience* **2021**, *24*, 102332. [[CrossRef](#)] [[PubMed](#)]
4. Zhao, J.; Rao, Z.; Huo, Y.; Liu, X.; Li, Y. Thermal management of cylindrical power battery module for extending the life of new energy electric vehicles. *Appl. Therm. Eng.* **2015**, *85*, 33–43. [[CrossRef](#)]
5. Pesaran, A. Battery thermal models for hybrid vehicle simulations. *J. Power Sources* **2002**, *110*, 377–382. [[CrossRef](#)]
6. Zeng, Y.; Chalise, D.; Lubner, S.; Kaur, S.; Prasher, R. A review of thermal physics and management inside lithium-ion batteries for high energy density and fast charging. *Energy Storage Mater.* **2021**, *41*, 264–288. [[CrossRef](#)]

7. Yu, Y.; Tang, A.; Chen, W.; Jia, H.; Jin, Y. Experimental Investigation of a Battery Thermal Management Device Based on a Composite Phase Change Material Coupled with a Double Helix Liquid Cooling Plate. *Energy Fuels* **2022**, *36*, 13370–13381. [[CrossRef](#)]
8. Choudhari, V.; Dhoble, A.; Panchal, S. Numerical analysis of different fin structures in phase change material module for battery thermal management system and its optimization. *Int. J. Heat Mass Transf.* **2020**, *163*, 120434. [[CrossRef](#)]
9. Landini, S.; Waser, R.; Stamatou, A.; Ravotti, R.; Worlitschek, J.; O'Donovan, T. Passive cooling of Li-Ion cells with direct-metal-laser-sintered aluminium heat exchangers filled with phase change materials. *Appl. Therm. Eng.* **2020**, *173*, 115238. [[CrossRef](#)]
10. Cao, J.; Luo, M.; Fang, X.; Ling, Z.; Zhang, Z. Liquid cooling with phase change materials for cylindrical Li-ion batteries: An experimental and numerical study. *Energy* **2020**, *191*, 116565. [[CrossRef](#)]
11. Hekmat, S.; Molaeimanesh, G. Hybrid thermal management of a Li-ion battery module with phase change material and cooling water pipes: An experimental investigation. *Appl. Therm. Eng.* **2020**, *166*, 114759. [[CrossRef](#)]
12. Zhang, X.; Li, Z.; Luo, L.; Fan, Y.; Du, Z. A review on thermal management of lithium-ion batteries for electric vehicles. *Energy* **2022**, *238*, 121652. [[CrossRef](#)]
13. Wang, Y.; Jiang, J.; Chung, Y.; Chen, W.; Shu, C. Forced-air cooling system for large-scale lithium-ion battery modules during charge and discharge processes. *J. Therm. Anal. Calorim.* **2018**, *135*, 2891–2901. [[CrossRef](#)]
14. Sharma, A.; Patil, Y.; Krishnaiah, R.; Ashok, B.; Garg, A.; Gao, L. Study on effect of diverse air inlet arrangement on thermal management of cylindrical lithium-ion cells. *Heat Transf.* **2020**, *49*, 4626–4656. [[CrossRef](#)]
15. Xi, Y.; Feng, Y.; Xiao, Y.; He, G. Novel Z-Shaped Structure of Lithium-Ion Battery Packs and Optimization for Thermal Management. *J. Energy Eng.* **2020**, *146*, 04019035. [[CrossRef](#)]
16. Liu, Y.; Zhang, J. Design a J-type air-based battery thermal management system through surrogate-based optimization. *Appl. Energy* **2019**, *252*, 113426. [[CrossRef](#)]
17. Mohammed, A.; Elfeky, K.; Wang, Q. Recent advancement and enhanced battery performance using phase change materials based hybrid battery thermal management for electric vehicles. *Renew. Sustain. Energy Rev.* **2022**, *154*, 111759. [[CrossRef](#)]
18. Zhao, C.; Cao, W.; Dong, T.; Jiang, F. Thermal behavior study of discharging/charging cylindrical lithium-ion battery module cooled by channeled liquid flow. *Int. J. Heat Mass Transf.* **2018**, *120*, 751–762. [[CrossRef](#)]
19. Zhao, C.; Sousa, A.; Jiang, F. Minimization of thermal non-uniformity in lithium-ion battery pack cooled by channeled liquid flow. *Int. J. Heat Mass Transf.* **2019**, *129*, 660–670. [[CrossRef](#)]
20. Xu, H.; Zhang, X.; Xiang, G.; Li, H. Optimization of liquid cooling and heat dissipation system of lithium-ion battery packs of automobile. *Case Stud. Therm. Eng.* **2021**, *26*, 101012. [[CrossRef](#)]
21. Zhou, H.; Zhou, F.; Zhang, Q.; Wang, Q.; Song, Z. Thermal management of cylindrical lithium-ion battery based on a liquid cooling method with half-helical duct. *Appl. Therm. Eng.* **2019**, *162*, 114257. [[CrossRef](#)]
22. Dong, F.; Cheng, Z.; Zhu, J.; Song, D.; Ni, J. Investigation and optimization on cooling performance of a novel double helix structure for cylindrical lithium-ion batteries. *Appl. Therm. Eng.* **2021**, *189*, 116758. [[CrossRef](#)]
23. Rao, Z.; Qian, Z.; Kuang, Y.; Li, Y. Thermal performance of liquid cooling based thermal management system for cylindrical lithium-ion battery module with variable contact surface. *Appl. Therm. Eng.* **2017**, *123*, 1514–1522. [[CrossRef](#)]
24. Lai, Y.; Wu, W.; Chen, K.; Wang, S.; Xin, C. A compact and lightweight liquid-cooled thermal management solution for cylindrical lithium-ion power battery pack. *Int. J. Heat Mass Transf.* **2019**, *144*, 118581. [[CrossRef](#)]
25. Sheng, L.; Zhang, H.; Su, L.; Zhang, Z.; Zhang, H.; Li, K.; Fang, Y.; Ye, W. Effect analysis on thermal profile management of a cylindrical lithium-ion battery utilizing a cellular liquid cooling jacket. *Energy* **2021**, *220*, 119725. [[CrossRef](#)]
26. Zhao, J.; Rao, Z.; Li, Y. Thermal performance of mini-channel liquid cooled cylinder based battery thermal management for cylindrical lithium-ion power battery. *Energy Convers. Manag.* **2015**, *103*, 157–165. [[CrossRef](#)]
27. Reddy, T.; Linden, D. *Linden's Handbook of Batteries*, 4th ed.; McGraw-Hill: New York, NY, USA, 2010; pp. 23–26, 967.
28. Parsons, K.; Mackin, T. Design and Simulation of Passive Thermal Management System for Lithium-Ion Battery Packs on an Unmanned Ground Vehicle. *J. Therm. Sci. Eng. Appl.* **2016**, *9*, 011012. [[CrossRef](#)]
29. Cheng, E.; Taylor, N.; Wolfenstine, J.; Sakamoto, J. Elastic properties of lithium cobalt oxide (LiCoO<sub>2</sub>). *J. Asian Ceram. Soc.* **2017**, *5*, 113–117. [[CrossRef](#)]
30. Tang, W.; Tam, W.C.; Yuan, L.; Dubaniewicz, T.; Thomas, R.; Soles, J. Estimation of the critical external heat leading to the failure of lithium-ion batteries. *Appl. Therm. Eng.* **2020**, *179*, 115665. [[CrossRef](#)]
31. Gu, L.; Han, J.; Chen, M.; Zhou, W.; Wang, X.; Xu, M.; Lin, H.; Liu, H.; Chen, H.; Chen, J.; et al. Enabling robust structural and interfacial stability of micron-si anode toward high-performance liquid and solid-state lithium-ion batteries. *Energy Storage Mater.* **2022**, *52*, 547–561. [[CrossRef](#)]
32. Han, X.; Zhou, W.; Chen, M.; Chen, J.; Wang, G.; Liu, B.; Luo, L.; Chen, S.; Zhang, Q.; Shi, S.; et al. Interfacial nitrogen engineering of robust silicon/mxene anode toward high energy solid-state lithium-ion batteries. *J. Energy Chem.* **2022**, *67*, 727–735. [[CrossRef](#)]
33. Primary and Rechargeable Battery Chemistries with Energy Density. Available online: <https://www.epectec.com/batteries/chemistry/> (accessed on 13 July 2022).
34. Zhao, R.; Liu, J.; Gu, J. Simulation and experimental study on Lithium Ion Battery Short Circuit. *Appl. Energy* **2016**, *173*, 29–39. [[CrossRef](#)]

35. Kukreja, J.; Nguyen, T.; Siegmund, T.; Chen, W.; Tsutsui, W.; Balakrishnan, K.; Liao, H.; Parab, N. Crash analysis of a conceptual electric vehicle with a damage tolerant battery pack. *Extrem. Mech. Lett.* **2016**, *9*, 371–378. [[CrossRef](#)]
36. Qian, Z.; Li, Y.; Rao, Z. Thermal performance of lithium-ion battery thermal management system by using mini-channel cooling. *Energy Convers. Manag.* **2016**, *126*, 622–631. [[CrossRef](#)]
37. Bernardi, D.; Pawlikowski, E.; Newman, J. A General Energy Balance for Battery Systems. *J. Electrochem. Soc.* **1985**, *132*, 5–12. [[CrossRef](#)]
38. Huang, Y.; Lu, Y.; Huang, R.; Chen, J.; Chen, F.; Liu, Z.; Yu, X.; Roskilly, A.P. Study on the thermal interaction and heat dissipation of cylindrical Lithium-Ion Battery cells. *Energy Procedia* **2017**, *142*, 4029–4036. [[CrossRef](#)]
39. Walvekar, H.; Beltran, H.; Sripad, S.; Pecht, M. Implications of the Electric Vehicle Manufacturers’ Decision to Mass Adopt Lithium-Iron Phosphate Batteries. *IEEE Access* **2022**, *10*, 63834–63843. [[CrossRef](#)]
40. Wang, Z.; Li, X.; Zhang, G.; Lv, Y.; Wang, C.; He, F.; Yang, C.; Yang, C. Thermal management investigation for lithium-ion battery module with different phase change materials. *RSC Adv.* **2017**, *7*, 42909–42918. [[CrossRef](#)]
41. Sosnowski, M.; Krzywanski, J.; Grabowska, K.; Gnatowska, R. Polyhedral meshing in numerical analysis of conjugate heat transfer. *EPJ Web Conf.* **2018**, *180*, 02096. [[CrossRef](#)]
42. Shahid, S.; Agelin-Chaab, M. Development and analysis of a technique to improve air-cooling and temperature uniformity in a battery pack for cylindrical batteries. *Therm. Sci. Eng. Prog.* **2018**, *5*, 351–363. [[CrossRef](#)]
43. Inflation Layer Meshing in ANSYS. Available online: <https://www.computationalfluidynamics.com.au/tips-tricks-inflation-layer-meshing-in-ansys/> (accessed on 2 July 2022).
44. ANSYS, Inc. *ANSYS Fluent User’s Guide*; ANSYS, Inc.: Canonsburg, PA, USA, 2021; pp. 972–973.
45. Yates, M.; Akrami, M.; Javadi, A. Analysing the performance of liquid cooling designs in cylindrical lithium-ion batteries. *J. Energy Storage* **2021**, *33*, 100913. [[CrossRef](#)]
46. Bai, F.; Chen, M.; Song, W.; Feng, Z.; Li, Y.; Ding, Y. Thermal management performances of PCM/water cooling-plate using for lithium-ion battery module based on non-uniform internal heat source. *Appl. Therm. Eng.* **2017**, *126*, 17–27. [[CrossRef](#)]
47. Chen, D.; Jiang, J.; Kim, G.; Yang, C.; Pesaran, A. Comparison of different cooling methods for lithium ion battery cells. *Appl. Therm. Eng.* **2016**, *94*, 846–854. [[CrossRef](#)]